



Analysis of ozone vertical profile day-to-day variability in the lower troposphere during the Paris-2022 ACROSS campaign

G rard Ancellet¹, Camille Viatte¹, Anne Boynard^{1,2}, Fran ois Ravetta¹, Jacques Pelon¹,
Cristelle Cailteau-Fischbach¹, Pascal Genau¹, Julie Capo³, Axel Roy³, and Philippe N d lec⁴

¹LATMOS, Sorbonne Universit , Universit  Versailles St-Quentin, CNRS/INSU, Paris, France

³CNRM, Universit  de Toulouse, M t o-France, CNRS, Toulouse, France

⁴Laboratoire d' A rologie, CNRS and Universit  Toulouse III, Paul Sabatier, Toulouse, France

²SPASCIA, Ramonville-Saint-Agne, 31520, France

Correspondence: G rard Ancellet (gerard.ancellet@latmos.ipsl.fr)

Abstract. The ozone vertical profiles variability in the lower troposphere is analyzed during the summer 2022 ACROSS (Atmospheric ChemistRy Of the Suburban foreSt) measurement campaign as part of the PANAME (Paris region urbaN Atmospheric observations and models for Multidisciplinary rEsearch) project. The analysis is based on 21 days of Differential Absorption Lidar (DIAL) observations, in addition to the two daily vertical ozone profiles measured by In-service Aircraft for a Global Observing System (IAGOS) flights to and from Paris airport. The ACROSS ozone profiles are also a good opportunity to assess the lowermost tropospheric ozone column retrieval by the satellite observations of Infrared Atmospheric Sounding Interferometer (IASI). The planetary boundary layer (PBL) vertical structure evolution is monitored using a 808-nm microlidar and meteorological radiosondes launched in the city center. Characterization of the regional transport of polluted air masses advected over the city is based on the daily ozone analysis of the Copernicus Atmospheric Service (CAMS) ensemble model and on backward trajectories of the Paris city plume. This work show that the CAMS simulations of the Paris ozone plume between the surface and 3 km are consistent with the ACROSS ozone vertical profiles and that the IASI satellite observations can capture the day to day variability of the 0-3 km lowermost ozone column if the contribution of the surface column below 1.2 km is lower than 4 DU. The day time ozone vertical structure above the city center is also in good agreement with the PBL growth during the day and with the formation of the residual layer during the night. The O₃ DIAL may provide additional information about the PBL vertical structure to discuss differences between microlidar and radiosounding measurements of the PBL height.

In addition to the well-known control of the ozone photochemical production by atmospheric temperature, cloud cover and mixing between the surface layer (0 - 500 m) and the residual layer, the comparison of four ozone pollution events shows that the thickness of the PBL during the day and the advection of regional scale plumes above the PBL can significantly change the ozone concentrations above Paris city center. With similar cloud cover and air temperature, high ozone concentrations up to 180 $\mu\text{g}\cdot\text{m}^{-3}$ are encountered during the day when PBL height is below 1.5 km, while they remain below 150 $\mu\text{g}\cdot\text{m}^{-3}$ when PBL height increases above 2.5 km. Advection of ozone poor concentrations in the free troposphere during a Saharan dust event is able to mitigate the ozone photochemical production. On the other hand, the advection of a continental pollution plume with



high ozone concentrations $> 140 \mu\text{g}\cdot\text{m}^{-3}$ maintained high concentrations in the surface layer despite a temperature decrease
25 and cloud cover development.

1 Introduction

Ozone pollution poses significant challenges for air quality management during summer due to its harmful effects on human health and ecosystems (Fowler et al., 2008). As a secondary pollutant, ozone results from the interaction of sunlight with primary pollutants like nitrogen oxides (NO_x) and volatile organic compounds (VOCs), summer months being most conducive
30 to its formation (Monks et al., 2015). These interactions are strongly influenced by atmospheric conditions, which vary within the planetary boundary layer (PBL), the part of the atmosphere where the surface emissions directly affects weather and air quality. Vertical profiling of ozone within the PBL is essential for several reasons. Firstly, the production and destruction of ozone at different altitudes in the PBL depend on the vertical distribution of precursor chemicals and meteorological conditions (Zaveri et al., 2003). Secondly, vertical transport processes within the PBL, such as turbulent mixing and convective uplift,
35 significantly impact the distribution and concentration of ozone and its precursors (Seinfeld and Pandis, 2016). Thirdly the ozone plume from urban centers in the context of megacities, where large volumes of pollutants are emitted, can be transported across urban scales and can influence regional air quality significantly. For instance, the interplay between local emission sources in large urban areas and regional meteorological patterns can result in the formation of extensive ozone plumes that affect large geographical regions (Couillard et al., 2021; Ma et al., 2021). The summer 2022 ACROSS (Atmospheric ChemistRy
40 Of the Suburban foreSt) measurement campaign as part of the PANAME (PARis region urbaN Atmospheric observations and models for Multidisciplinary rEsearch) project employs advanced techniques like ozone lidar, backscatter microlidar, Doppler lidar, radiosounding and aircraft measurements to characterize the vertical structure of the low troposphere in the Paris city center area. This approach enables us to dissect the complex interactions between ozone, its precursors, and meteorological factors at various altitudes in the PBL. The ozone data gathered provides insights into the mechanisms driving pollution
45 episodes and aids in the identification of primary factors contributing to high ozone events.

Over the past two decades several campaigns have focused on understanding ozone pollution episodes in cities. The “Etude et Simulation de la Qualite de l’air en Île-de-France” ESQUIF project was conducted in the Paris region (Vautard et al., 2003), the main focus being the analysis of the contrast between summer and winter conditions in the relative contribution local ozone photochemistry compared to regional transport. The ESQUIF campaign results demonstrated that the Paris area was well suited
50 to study the urban heat island (UHI) effect in pollutant distribution due to enhanced turbulence inside boundary layer (Sarrat et al., 2006). During the ESCOMPTE campaign held in 2001, the focus was on the fate of the Marseille area urban and industrial emissions on ozone formation in the context of very complex meteorological conditions with land-sea breeze and orographic effects (Drobinski et al., 2007). Ground based UV DIAL ozone lidar and aircraft observations demonstrated the sensitivity of the lowermost tropospheric vertical ozone distribution to mesoscale dynamical processes (Ancellet and Ravetta, 2005).
55 Several campaigns took place in North America to characterize high ozone summer concentrations observed in Southeastern US and in California: Texas Air Quality Study in 2000 and 2006 (TexAQS) in 2000 and 2006 (Daum et al., 2004; Senff et al.,



2010), California Research at the Nexus of Air Quality and Climate Change (CalNex) (Ryerson et al., 2013), During these campaigns extensive use of aircraft and lidar were conducted to better understand the sources and formation mechanism of O₃ plumes, showing that meteorology and boundary layer heights are significant parameters influencing the vertical distribution of ozone in these areas. Results of these campaigns also demonstrated that residual layer ozone reincorporation with mixed layer development contributes to a significant part of surface ozone concentration increase in the afternoon. Contribution of long range transport of ozone has been also analyzed using airborne differential absorption LIDAR (DIAL) and satellite. For example it was shown that regional transport of ozone from Asian emissions over the North Pacific Ocean to California is responsible for a significant part of lower tropospheric ozone increase in Summer (Lin et al., 2012).

In the present paper the focus will be again on the Paris area taking advantage of the ACROSS campaign held in Summer 2022 with numerous aircraft flights around Paris and several remote sensing lidar and radar observations carried out in June and July. Several ozone pollution episodes have been encountered during this period. The presentation of the ozone vertical observations available during this period as well as a first analysis of the respective contribution of the urban boundary layer structure and of the ozone plume regional transport are the main objectives of this paper. The overall description of the ozone variability during the ACROSS campaign and the selection of the pollution events analyzed in this work are presented in section 3. The presentation of the data set in section 4 is mainly about the analysis of lidar observations. The comparison of the ACROSS ozone vertical profiles and satellite observations, as well as a comparison of the pollution events in term of regional ozone transport and PBL dynamical development are discussed in section 5.

2 Description of observation and modelling tools

2.1 In-situ surface observations

Numerous observations are available in the Paris area to monitor hourly-averaged ozone concentration and temperature. We will focus in this work on three monitoring sites located in (i) the Paris 13 station located at 60 m ASL in a park not directly influenced by traffic emissions, (ii) the top of the QUALAIR University Zamansky tower at 125 m ASL (iii) the 3rd floor of the Eiffel tower at 310 m ASL (Fig. 1). Since no temperature are available at the Paris 13 station, the Luxembourg park temperature at 46 m ASL has been used to characterize the surface temperature. The accuracy of the O₃ measurements is around 5 µg.m⁻³. The tower observations have been used to characterize the temporal evolution of the surface layer lapse rate and the ozone vertical gradient near the surface. The latter is very useful to measure the O₃ vertical profile down to the ground as the QUALAIR lidar is blind below 250 m AGL.

2.2 O₃ vertical profiles

The observations discussed in this work have been carried out during the ACROSS campaign from June 13, 2022 to July 13, 2022. Ozone vertical profiles are obtained from a UV DIAL instrument installed on the Sorbonne Université campus. The instrument is described in Klein et al. (2017); Ancellet and Ravetta (1998) and provide observations in the altitude range 0.3 to



5 km during nighttime and up to 2.7 km during daytime. Only daytime measurements have been carried out during ACROSS-2022 as the lidar could not be remotely controlled during this campaign. Although the DIAL sampling rate is 15 s, the ozone vertical profiles are usually hourly-averages to match the surface data time resolution and to improve the lidar signal-to-noise ratio above the planetary boundary layer top. The accuracy of the lidar observations is altitude-dependent being of the order of $7\mu\text{g}\cdot\text{m}^{-3}$ below 1000 m and occasionally increases up to $20\mu\text{g}\cdot\text{m}^{-3}$ above 2 km at midday. The latter is due to elevated background skylight noise at noon or to a reduction in the number of averaged lidar shots during scattered cloud occurrence at altitudes below 2 km. The vertical resolution is less than 100 m at a 250-m altitude and of the order of 500 m at a 2500-m altitude.

Ozone in-situ measurements on IAGOS (In-service Aircraft for a Global Observing System) aircraft provide a vertical profile of ozone during take-off and landing at the Paris Charles de Gaulle (CDG) airport (Nédélec et al., 2015). Typical aircraft trajectories during landings (early morning flights before 6 UT) and take-offs (midday flights after 10 UT) are shown in the supplementary document (Fig. S1, S2). The horizontal domain, where the aircraft remains at altitudes of less than 3 km, does not exceed a radius of 40 km around CDG airport. The aircraft is never above the city center when it flies below 3 km. The aircraft location is generally northeast of Paris between 2.5° and 3° E during takeoff (afternoon flights) except on July 13 when the aircraft position is northwest of Paris. The aircraft positions during landing (early morning flights) are generally within a $20\text{km} \times 50\text{km}$ box either northwest or northeast of Paris. The accuracy of the IAGOS O_3 measurements is better than ± 2 ppbv/ $\pm 2\%$ (Thouret et al., 1998) and the vertical resolution of the O_3 profile is of the order of 30 m. The respective positions of the O_3 DIAL and of the CDG airport are shown in Fig. 1.

2.3 PBL height characterization

Two instruments have been used to characterize the PBL evolution nearby the QUALAIR ozone lidar: an autonomous 808-nm microlidar (SLIM) derived from the IAOOS instrument developed by CIMEL and LATMOS (Pelon et al., 2008; Mariage et al., 2017) and meteorological radiosondes launched 4 times a day for 6 days of pollution in June 2022. The SLIM lidar is routinely operated at Jussieu QUALAIR facility on a 24-hour/7-day basis. It provided observations during the full ACROSS campaign using an automated procedure. In this procedure, the raw backscattered signal is first normalized using the integrated attenuated backscatter signal on water cloud layers (O'Connor et al., 2004). The attenuated backscatter signal is derived from the SLIM lidar signal after calibration and correction of the geometrical factor (Pelon et al., 2008; Mariage et al., 2017). The attenuated backscatter is used to identify clouds on the basis of a lidar signal attenuated backscatter above a predefined threshold ($0.25\text{ km}^{-1}\text{sr}^{-1}$). It is then inverted to derive the backscattering coefficient in aerosol regions using a forward inversion procedure (Klett, 1985). A standard lidar ratio value of 40 sr is used corresponding to urban aerosol. Further refinements in the analysis can be performed to derive more accurate aerosol and cloud optical properties, but are not used here. The analysis is performed on one (the acquisition time) and ten minutes files.

The PBL height and the top of the residual boundary layer (RBL or RL, which is remain of the previous PBL development) are derived from the vertical structure of the aerosol backscattering coefficient and its variance as markers of the turbulent activity developed in the unstable summer boundary layer (Stull, 1988). A simple approach based on the analysis of the



gradients is used following previous studies (Dupont et al., 1994; Flamant and Pelon, 1996; Menut et al., 1999). A combination of information is used to mix backscattering and variance-derived heights in order to identify PBL and RL heights. It requires that significant vertical motions can be identified, as it is the case during daytime. The signature of such dynamics in the lidar signal is a coincident variance peak and a backscattering gradient (Menut et al., 1999). In the decay phase, or in the nocturnal layer development, the PBL height can be estimated from the variance as linked to residual turbulence activity (Stull, 1988). The RL height can be derived from the backscattering coefficient gradient, as particles are maintained in the atmosphere close to the maximum height (depending on particle size and subsidence) reached by the PBL during the day (or the day before for the morning period).

The meteorological radiosondes have been used to plot the thermodynamic skew-T diagram in order to determine the depth of the layer limited by the adiabatic ascent. It also allows to capture the lifting condensation level (LCL) where cloud base can be expected and level of free convection (LFC) above which fast vertical motion and deep convection can occur. The python library metpy.calc.lcl has been used for the automatic retrieval of LFC and LCL. It is complementary to the SLIM estimate of the PBL vertical structure. The SLIM lidar and the radiosounding site locations are shown in the Fig. 1.

2.4 Satellite observations: IASI

IASI (Infrared atmospheric sounding interferometer) is a nadir-viewing spectrometer (Clerbaux et al., 2009) that records the thermal infrared emission of the Earth-atmosphere system between 645 and 2760 cm^{-1} from the polar Sun-synchronous orbiting meteorological Metop series of satellites. Metop-A, -B and -C were successively launched in October 2006, September 2012 and November 2018. IASI provides global coverage of the Earth twice a day (at 9:30 and 21:30 mean local solar time) with a set of four simultaneous footprints of 12 km diameter on the ground at nadir. Thanks to IASI high spectral resolution of 0.5 cm^{-1} and a low radiometric noise below 0.4 K, vertical composition of various trace gases such as ozone can be assessed in the troposphere (Eremenko et al., 2008; Boynard et al., 2009; Viatte et al., 2011; Safieddine et al., 2013; Wespes et al., 2018).

In this study, we use the IASI O_3 profiles retrieved from the FORLI (Fast Optimal Retrievals on Layers for IASI) algorithm (Hurtmans et al., 2012) that can be downloaded from the AERIS portal (<http://iasi.aeris-data.fr/O3/>; Aeris, 2024). The FORLI- O_3 products (profiles and columns) have undergone a series of validation using available ground-based, aircraft, ozonesonde and other satellite observations over local areas and/or short time periods (Antón et al., 2011; Dufour et al., 2010; Pommier et al., 2012) and more recently at global scale over a 10-years period (Boynard et al., 2016, 2018; Keppens et al., 2018). IASI data and ozonesonde measurements are in agreement in the troposphere at mid-latitudes (differences of 11-13%) with a significant vertical sensitivity in the troposphere (Boynard et al., 2018). For this work, IASI/Metop-B and -C pixels located within the ACROSS domain (48.84°N-49°N, 2°E-2.5°E) associated with a fractional cloud coverage of 13% or less and filtered by retrieval quality flags (see Boynard et al. (2018)) have been selected. The O_3 0-3 km partial columns can be retrieved for both morning (\approx 9:30 LT, called AM) and evening (\approx 21:30 LT, called PM) overpasses.

2.5 CAMS ozone plume modelling

Copernicus Atmosphere Monitoring Service (CAMS) provides ENSEMBLE model hourly analysis of O₃ concentration at 5
155 levels (500m, 750m, 1000m, 2000m, 3000m) with an horizontal resolution of 10 x 10 km. Up to eleven air quality models are
used to build the ENSEMBLE analysis reducing the sensitivity to model error (Marécal et al., 2015; Inness et al., 2019). In this
work analysis have been used at 3 daily time steps 6 UT, 12 UT and 18 UT to map the ozone plume positions over Northern
France. The ozone ENSEMBLE analysis products have been downloaded in october 2023 for the ACROSS-2022 campaign
period between June 13 and July 13. The quality of the tropospheric ozone CAMS daily analysis is generally in good agreement
160 with ozonesondes and IAGOS aircraft observations at Northern mid-latitudes especially to simulate the formation of regional
ozone plumes during the summer (Wagner et al., 2021).

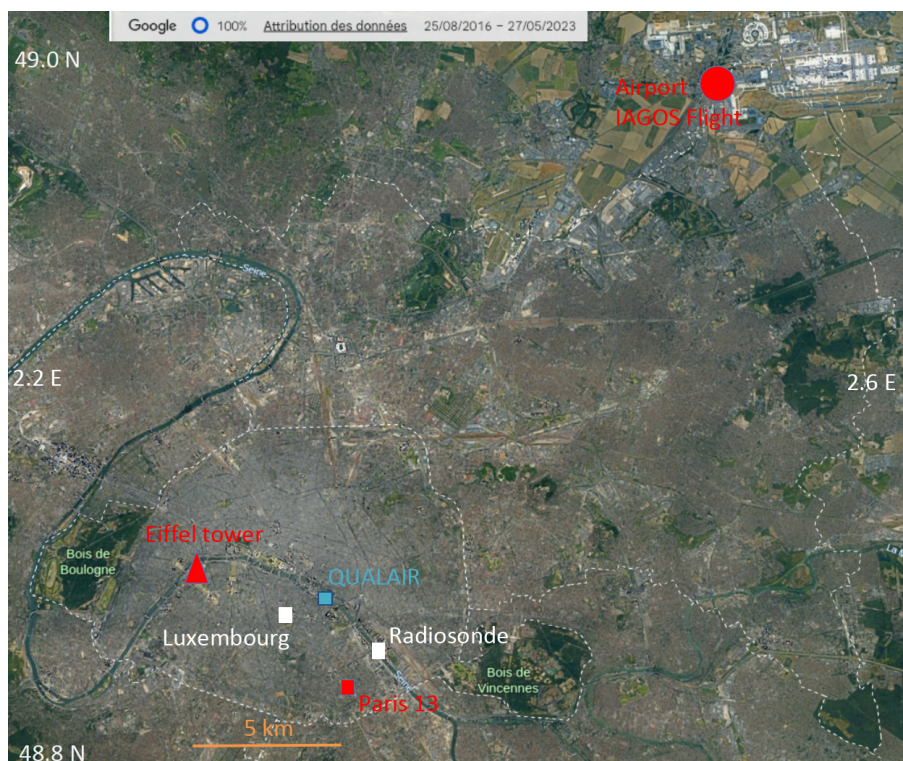


Figure 1. Map of ozone and meteorological measurement positions during the ACROSS-2022 experiment. The blue mark is the position of the QUALAIR station including the O₃ DIAL (33m ASL) and instruments operated on the top of the University Zamansky tower (125 m ASL). The red triangle is the position of the Eiffel tower 3rd platform (310 m ASL), the red square is the AIRPARIF PARIS 13 in-situ O₃ monitor in Parc de Choisy (50 m ASL), and the red circle is the IAGOS aircraft take-off and landing airport. White squares show the positions of the Parc du Luxembourg surface meteorological station (46 m) and of the meteorological radiosounding station. The map has been made with © Google Earth.



3 Selection of the ozone measurement period

The ACROSS-2022 campaign took place during three interesting periods with ozone concentrations above $100 \mu\text{g}\cdot\text{m}^{-3}$ and surface temperature above 30°C . The time evolution of the surface hourly ozone and temperature means are shown in Fig. 2 for the 3 stations located at different altitude levels between 40m and 310m ASL. Twelve days corresponding to the red arrows in Fig. 2 have been chosen to determine how the characterization of vertical ozone profiles and the spatial distribution of the pollution plume on a regional scale can be used to better intercompare these different ozone pollution episodes. Unfortunately no lidar data are available after July 14, e.g. during the ozone pollution episode on July 18. This is why this last pollution event is not considered in this work. The 500m-CAMS ozone distribution is a good proxy to track the day to day spatial distribution of the ozone plume at the regional scale, this plume being related to both the regional emissions of Western Europe and the urban emissions from the Paris area. They are shown at 18 UT when ozone concentrations reach their daily maximum in Fig.3 and 4 for the 12 days identified in Fig.2. The first period with elevated ozone concentrations took place from June 14 to June 18. This period was characterized by the highest ozone concentrations ($170 \mu\text{g}\cdot\text{m}^{-3}$) recorded within the city center, but also by O_3 concentrations $>140 \mu\text{g}\cdot\text{m}^{-3}$ over a large fraction of Northern France according to the CAMS simulations (Fig. 3). The second time period from June 21 to June 28 is rather typical of summer sunny days with ground temperatures near 30°C and moderate ozone pollution of the order $110 \mu\text{g}\cdot\text{m}^{-3}$ on June 21, 22 and 28. The CAMS simulations show a well defined ozone plume west of Paris on June 21 and June 22 (Fig.4a,b) with O_3 concentrations approaching $150 \mu\text{g}\cdot\text{m}^{-3}$. June 28 is also interesting as the Paris city O_3 concentrations below 300m are similar to the June 21/22 episode, while the June 28 CAMS O_3 concentrations in the plume located North of Paris (Fig.4c) remain below $130 \mu\text{g}\cdot\text{m}^{-3}$. The third ozone pollution period took place on July 11 until July 13 with regional ozone plumes (Fig.4d,e,f) somewhat similar to the June 21/22 case study. The city center O_3 concentrations are however as high as $140 \mu\text{g}\cdot\text{m}^{-3}$ approaching the values encountered during the June 14/18 episode. Both the ozone and temperature vertical gradient between the surface and 300 m at the time of the daily maximum decrease on the last days of each pollution episode. Measuring the ozone vertical profiles by the UV DIAL and IAGOS aircraft above the top of the Eiffel Tower is mandatory to understand to what extent the structure and intensity of the ozone plume described by the CAMS simulations can explain the surface measurements in central Paris. A better understanding of the weakening of the surface ozone vertical gradient between 0 and 300 m altitude will benefit also from the lidar and aircraft observations at altitudes above 300 m.

4 The vertical profile datasets

4.1 Boundary layer diurnal variation

An ozone layer is generally observed during the morning hours above the nocturnal surface layer in the RL (Neu et al., 1994; Klein et al., 2019). It is generally an ozone reservoir with limited NO_x titration and ozone deposition. This ozone-rich air in the RL can be mixed down into the surface boundary layer effectively (Caputi et al., 2019). The analysis of the boundary layer height diurnal variation using the microlidar SLIM is necessary to characterize the PBL growth during the day and the

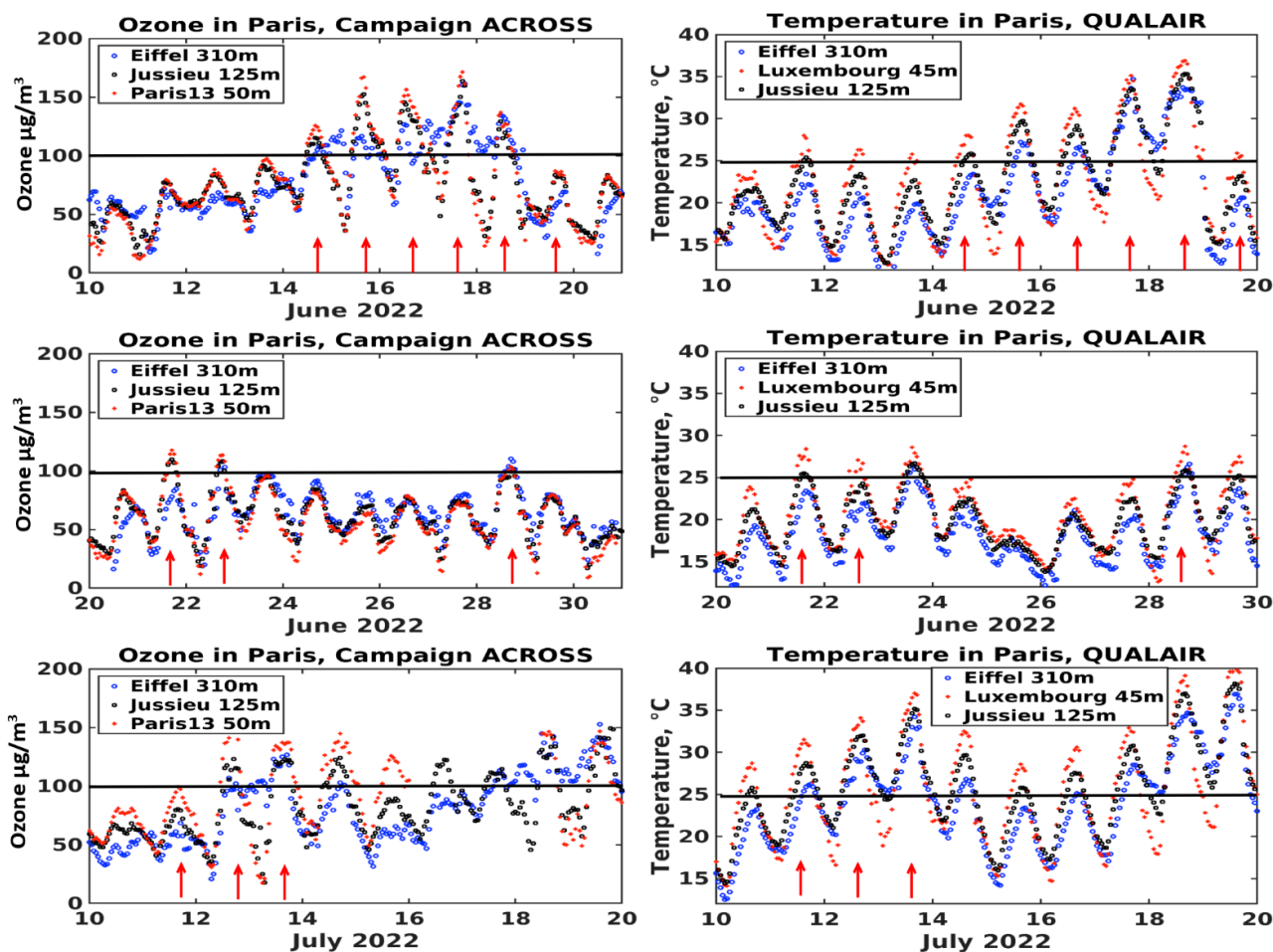


Figure 2. Surface O₃ concentration and temperature 10-day time evolution of the hourly mean during the ACROSS-2022 campaign in blue for the Eiffel tower top (310 m ASL), in black for the University Zamansky tower top (125 m ASL) and in red for the Paris 13 ozone sensor and for the Luxembourg park meteorological station (50 m). Days selected for the analysis of O₃ pollution events are shown by the red arrows.

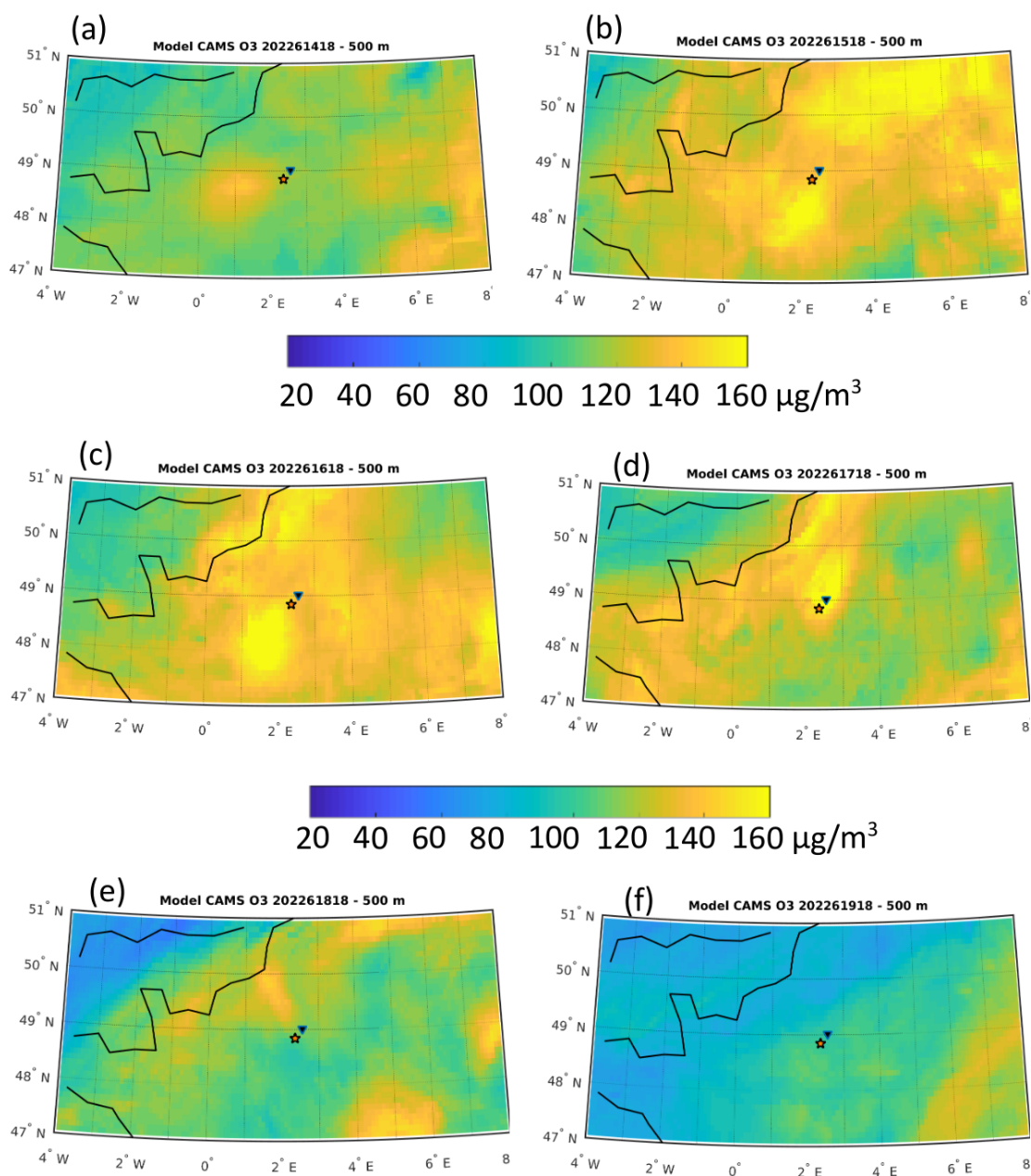


Figure 3. Ozone concentration distribution of the CAMS ensemble mean at 500 m above Northern France from June 14 (a) to June 19 (f), 2022 at 18 UT. The orange star and dark-blue triangle are respectively the DIAL position and the CDG airport. The color scale represents the O_3 concentration in $\mu\text{g}\cdot\text{m}^{-3}$.

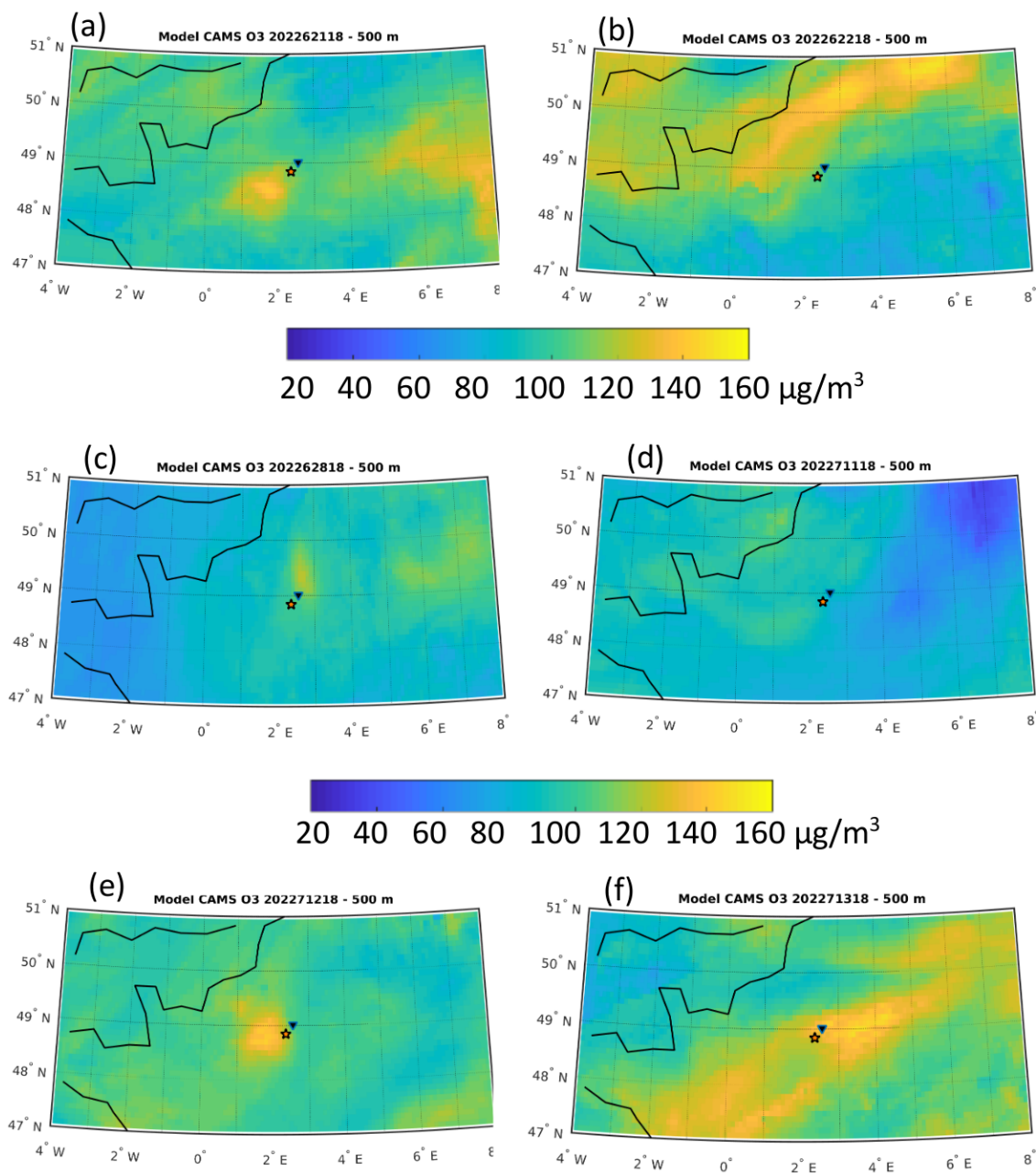


Figure 4. As Fig.3 for June 21 (a) to June 22 (b), June 28 (c) and July 11 (d) to 13 (f), 2022.

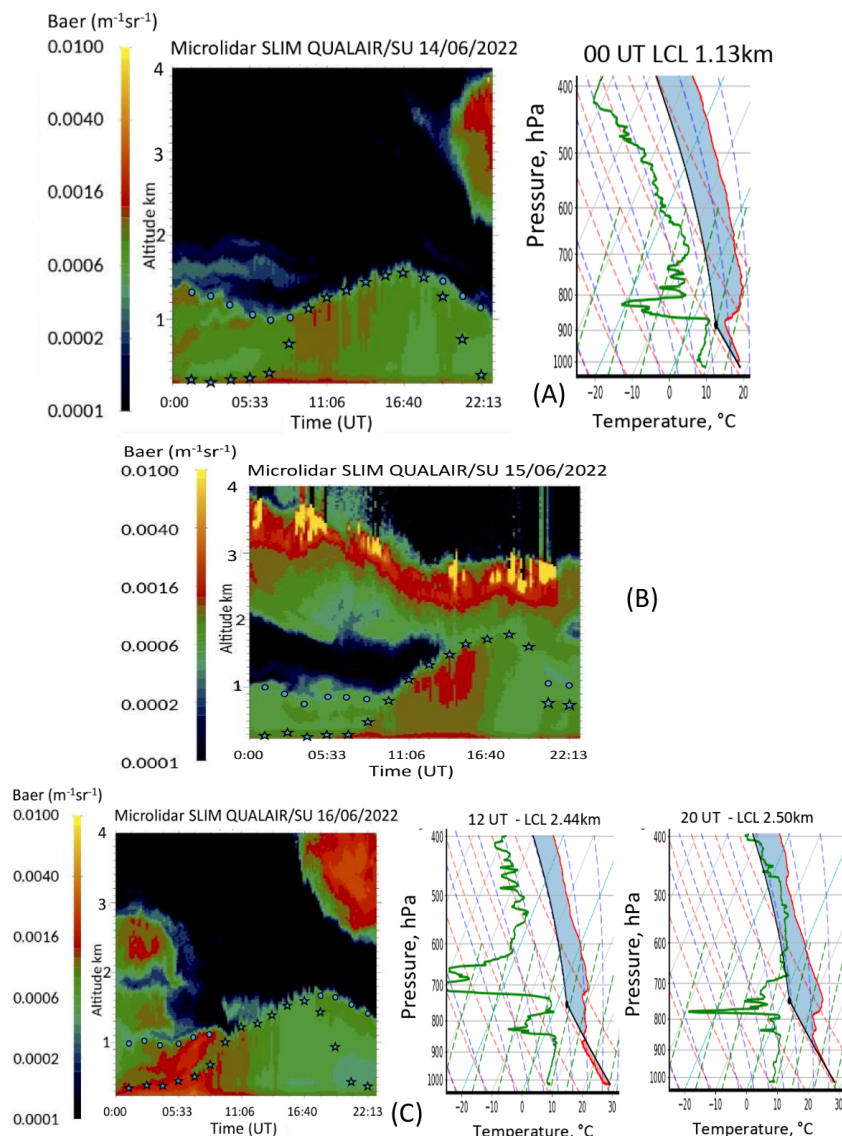


Figure 5. Color-coded diurnal evolution of the attenuated aerosol backscatter profiles measured by the 808-nm QUALAIR SLIM microlidar on June 14 (a), 15 (b) and 16 (c). The blue stars show the altitude of the convective boundary layer (CBL) top and the blue circles show the altitude of the residual layer top when the CBL decrease at the end of the day. Skew-T diagrams using radiosounding data are shown on June 14, 00 UT (a), June 16, 12 UT and 20 UT (c).

downward mixing of the RL. The diurnal variations of the 10-min aerosol backscatter vertical profiles measured by SLIM are shown in Fig.5 to 8 for the 12 days with elevated ozone concentrations. The PBL height (PBLH) and RL height (RLH) are derived using the methodology described in section 2.3 and are shown using respectively blue star and blue circle in Fig.5 to 8. These plots are also useful to identify the occurrence of long range transport of aerosol plumes in the free troposphere

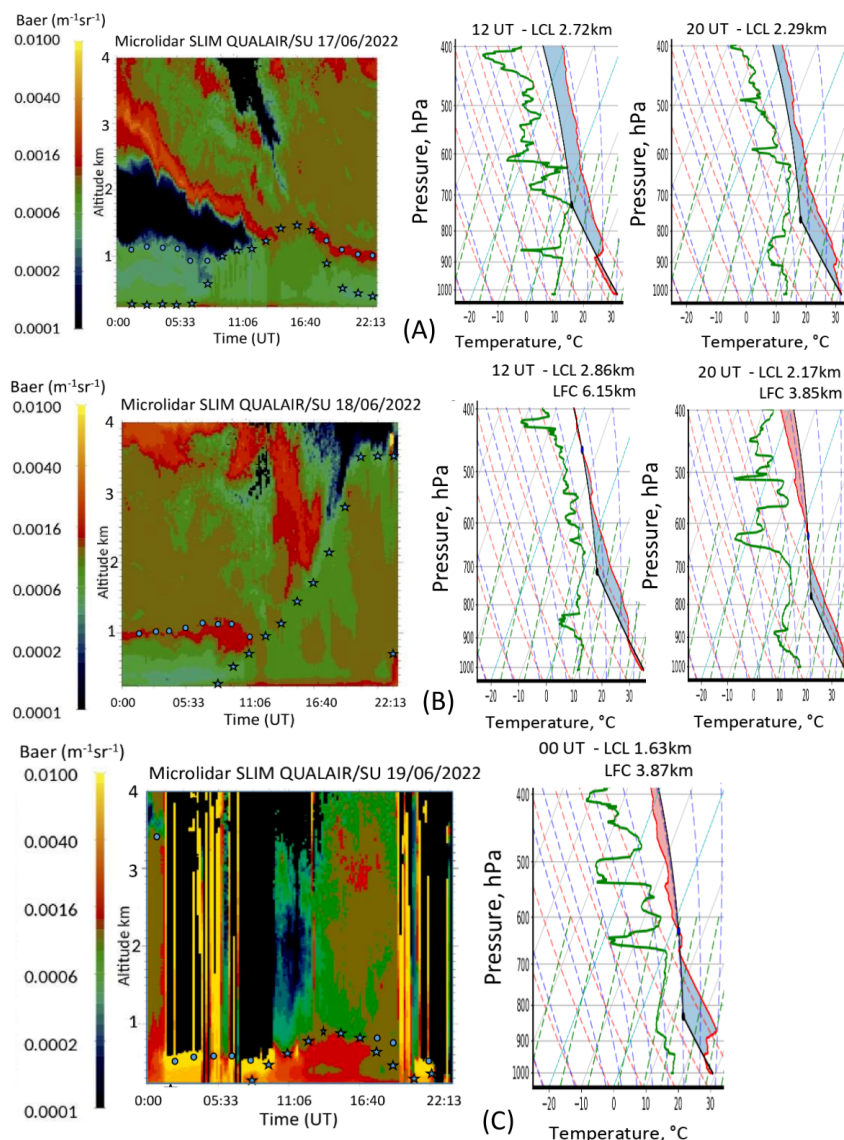


Figure 6. As Fig.5 for June 17 (a), 18 (b), 19 (c). Skew-T diagrams are shown at 12 UT, 20 UT on June 17 (a), 18 (b), and at 00 UT on June 19 (c). c

above the PBL, e.g. the Saharan dust plumes observed in the 2-4km altitude range from June 15 to June 18 (Fig.5b, Fig.6a,b) or the recirculation of the European continental aerosol (Fig.7a,b). The aerosol plume attribution was based on linear 532 nm depolarization ratio larger than 0.2 measured by the CIMEL lidar measurements of the QUALAIR station and based on long range transport modeling in section 5.2. Another interesting feature is the overall difference of the aerosol backscatter magnitude within the PBL when looking at the first (June 15-18) and at the last (July 12-13) heat wave episode. The latter with no dust plume aloft corresponds to less aerosol backscatter within the PBL. Large 808 nm aerosol backscatter values above

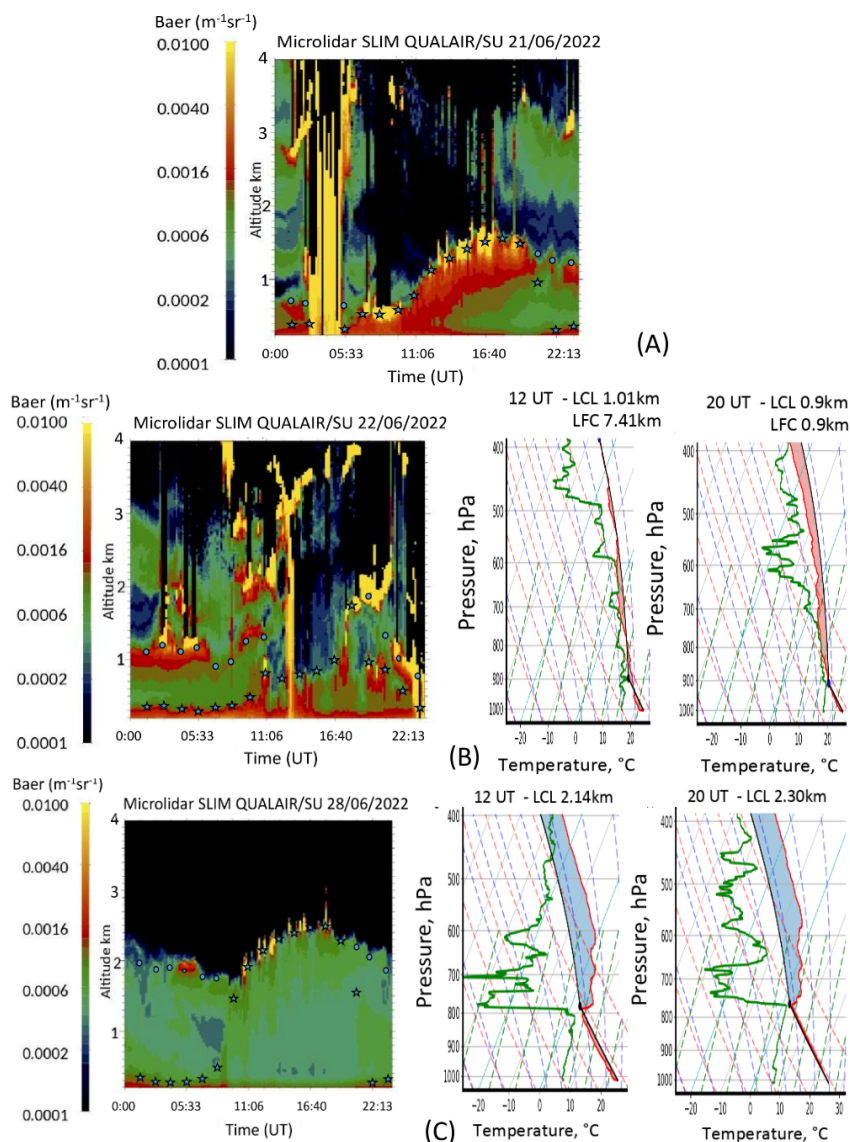


Figure 7. As Fig.5 for June 21 (a), 22 (b), 28 (c). Skew-T diagrams are shown at 12 UT, 20 UT on June 22 (b), June 28 (c).

0.01 km⁻¹sr⁻¹ (yellow pixels in Fig.5 to 8) correspond to cloud layer formation at the top or above the PBL. The 1-min high resolution cloud observations of the SLIM lidar have been also used to filter out the cloudy DIAL lidar observations when retrieving the ozone profile.

Data of the 16 meteorological radiosondes are also shown in Table 1 and in Fig.5 to 7 using thermodynamic skew-T diagrams. The bottom altitudes of inversion layers (ILH) detected by the radiosondes below 4 km shown in Table 1 are retrieved using layers with potential temperature vertical gradient larger than 15 K/km. They can be compared with the SLIM PBLH and RLH.

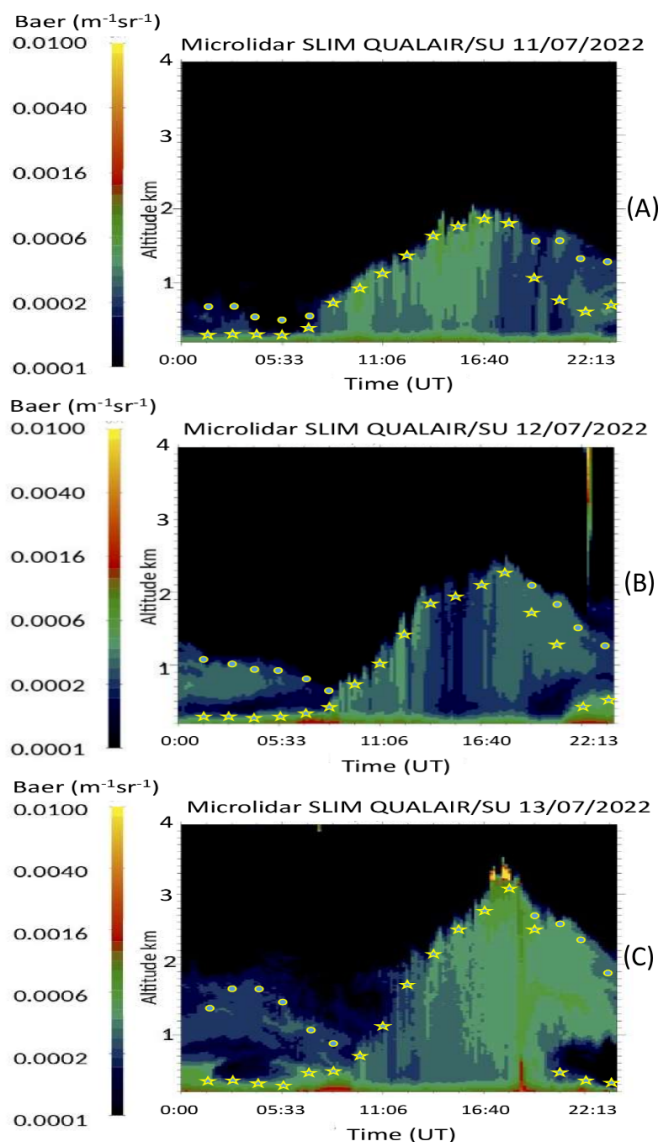


Figure 8. As Fig.5 for July 11 to 13, 2022. No radiosounding data are available for this episode.

210 There is a good agreement between both the lidar retrieval and the analysis of the meteorological radiosondes especially for the
timing of the PBL growth and the low thickness of the surface layer around 00 UT. The main differences are observed on June
22 when the atmospheric vertical stability was rapidly changing during the day and when some convective clouds developed
at 12:30 UT. Cloud occurrence is expected on this day according to the low values (≈ 1 km) of the lifting condensation
level (LCL) and the significant decrease of the level of free convection (LFC) during daytime (Fig.7b). The 2-km RLH height
215 observed by the lidar on June 22 in the evening is however consistent with the ILH observed by the radiosondes at 16 UT



Table 1. Comparison of the 808-nm microlidar SLIM Planetary Boundary Layer (PBL) and Residual Layer (RL) heights with the meteorological radiosounding inversion layer (IL) bottom altitudes observed below 4 km

Date	06/14			06/16			06/17			06/18			06/19			06/22			06/28		
Hour,UT	00	12	20	00	12	20	00	12	20	00	12	20	00	12	16	20	00	12	20		
First IL height,km	0.2	1.4	1.6	0.2	1.2	0.25*	0.2	1.0	0.3*	0.5	0.5*	0.8	1.0	0.4	2.1	2.3					
Second IL height,km	1.4		2.2			1.2		3.5	3.5	3.5	1.5*	2.0	3.8	2.4							
Lidar PBL height,km	0.3	1.3	1.0	0.25	1.2	0.5	0.25	1.0	3.5	0.25	0.7	0.9	1.0	0.4	2.1	1.6					
Lidar RL height,km	1.5		1.7	1.2		1.1	1.02			3.5			1.9	2.2		2.3					

*stable layer with thickness < 50 m

(Tab.1) when no cloud is present. The PBLHs generally remain below 2 km between June 14 and 22 (Fig.5,6,7a), except on June 18 with a fast rising of the PBLH in the evening (Fig.6c). The PBLHs however exceed the 2-km altitude level on June 28 (Fig.7c) and during the third pollution episode (Fig.8). It is likely related to a change in the atmospheric circulation due to a change in synoptic weather pattern with anticyclonic downward advection before June 22 and upward advection of marine air from the Atlantic ocean or the North sea on June 28 or on July 11 to 13 (see section 5.2). The largest PBLHs beyond 3 km have been observed on June 18 and July 13 for the highest surface temperatures above 35°C (Fig.2).

The daily maximum of the PBLH generally occurs around 17 UT, except on June 18 when it took place at 20:30 UT (Fig. 6b). However, PBLH and RLH decrease below 2 km at 23 UT despite high surface temperatures similar to those of June 18. Another interesting feature for the downward transport of ozone the following day is the occurrence of RL heights below 1.5 km at 21 UT, followed by a continuous decrease in RLHs after 21 UT. There are 4 days with such behavior: June 14, 16, 22 and July 12. These 4 days in fact correspond to high nighttime surface ozone concentrations above 100 µg.m⁻³ (Fig.2), consistent with an efficient downward mixing of RLs in the 0-300m surface layer during the night.

4.2 DIAL ozone diurnal variation

The ozone vertical profile are taken from the O₃ DIAL observations for the days selected in section 3. The time/altitude daytime evolution of the ozone concentration is shown in the left-hand columns of Fig.9 to Fig.12. Data from the surface stations shown in Fig.2 are also included to these figures using the same color-coded scale. They correspond to the pixels with the black cross in Fig.9 to Fig.12. The diurnal cycle observed by the Eiffel and Zamansky tower stations at 125 m and 310 m are consistent with the lidar observation at 300 ASL, following the previous study of Klein et al. (2017). CAMS vertical O₃ profiles are also retrieved using the ensemble model data at 5 vertical levels and within the box [48.84°N-49°N, 2°E-2.5°E]. The latter



235 corresponds to an horizontal domain of 36km x 17km including the QUALAIR station and the CDG Airport. The CAMS
vertical profiles are shown at 6 UT, 12 UT and 18 UT in the right-hand columns of Fig.9 to Fig.12. The first, last and midday
vertical profiles of the DIAL located in the city center plus the available IAGOS ozone vertical up to 3 km are also shown in
the right-hand columns of Fig.9 to Fig.12. Such a comparison of the three O₃ profiles is useful to check if the ozone layers
observed by the DIAL in the Paris city center is also present at the scale of the entire Paris Ile de France region and if advection
240 of the regional O₃ plume plays a significant role in the ozone diurnal variation in the city center. The PBLH and RLH diurnal
variation derived from results of section 4.1 are also included in the DIAL ozone time-altitude cross-sections (Fig.9 to 12) to
take into account the role of RL in the O₃ vertical profile diurnal variation, but also the possible downward mixing within the
PBL of ozone-rich or ozone-poor layers advected in the free troposphere above Western Europe.

The well-known early morning O₃ depletion due to the nighttime ozone deposition and NO_x titration (Güsten et al., 1998)
245 is observed up to 750 m by the DIAL with concentrations as low as 40 µg.m⁻³ before 9 UT. The daily maximum O₃ concen-
trations at the surface and the PBL top is always found after 14 UT when O₃ precursor gases are transported upward within
the PBL. The largest daily ozone concentrations (up to 175 µg.m⁻³) in the 500m-1000m altitude layer observed by the DIAL
on June 15 to June 17 correspond very well with the three days when elevated CAMS ozone concentrations larger than 140
µg.m⁻³ are present over a large part of Northern France according to Fig.3. The IAGOS and CAMS vertical profiles below
250 1 km in Fig.9d, 9f, 10b) show also the largest O₃ concentration observed over the Paris Ile de France area (150-160 µg.m⁻³)
from June 15 to 17. The two days with the lowest UV DIAL ozone concentration (below 100 µg.m⁻³) on June 28 and July
11 corresponds to a large fraction of Northern France with ozone daily maximum at 18 UT below 80 µg.m⁻³ (Fig.4c,d). The
IAGOS and CAMS O₃ vertical profiles also show concentrations below 100 µg.m⁻³ for these two days.

The depth of the afternoon O₃ layer is generally below 1.5 km and corresponds quite well with PBLH (blue star in Fig.9 to
255 12), except on June 19 and June 22 when the ozone layer extend up to 1.5 km while PBLH maximum remains below 1 km. On
June 22, PBLH might be underestimated by SLIM since on one hand, PBLH retrieved in section 4.1 rises up 2 km only after
17 UT despite the presence of an aerosol layer up to 2 km at 15 UT and on the other hand, the 16 UT meteorological sounding
identifies a well defined ILH at 2 km. The O₃ DIAL might help to clear up ambiguity about the PBLH value more in line with
the 16 UT radiosounding. On June 19, there is no reason to question the low PBLH of the microlidar SLIM, while advection of
260 the continental pollution plume above the PBL might very well explain the presence of the 130 µg.m⁻³ ozone layer between
1 and 1.5 km (see next section 5.2). There are only two days with both PBLH and DIAL ozone layer depth above 2 km: June
28 and July 13 when the IAGOS ozone concentrations reach 100 µg.m⁻³ above 2.5 km (Fig.11f, 12f).

The positions of the RLH (blue circle in Fig.9 to 12) are also in very good agreement with ozone concentrations generally
above 110 µg.m⁻³ observed early in the morning between 0.6 and 1.3 km. There are only two cases with O₃ concentrations
265 higher in the free troposphere than in the RL: June 22 when one layer with O₃ concentrations over 130 µg.m⁻³ is advected at
2 km and July 12 when a layer with O₃ concentration over 100 µg.m⁻³ is observed in the early morning hours at 1.5 km both
by the DIAL and IAGOS aircraft (Fig.12d).

Regarding the layers at altitude levels above the PBLH or the RLH, there are two periods with large differences in O₃
concentrations (≈ ±60 µg.m⁻³) measured in the free troposphere and in the PBL/RL. First low ozone concentrations less than

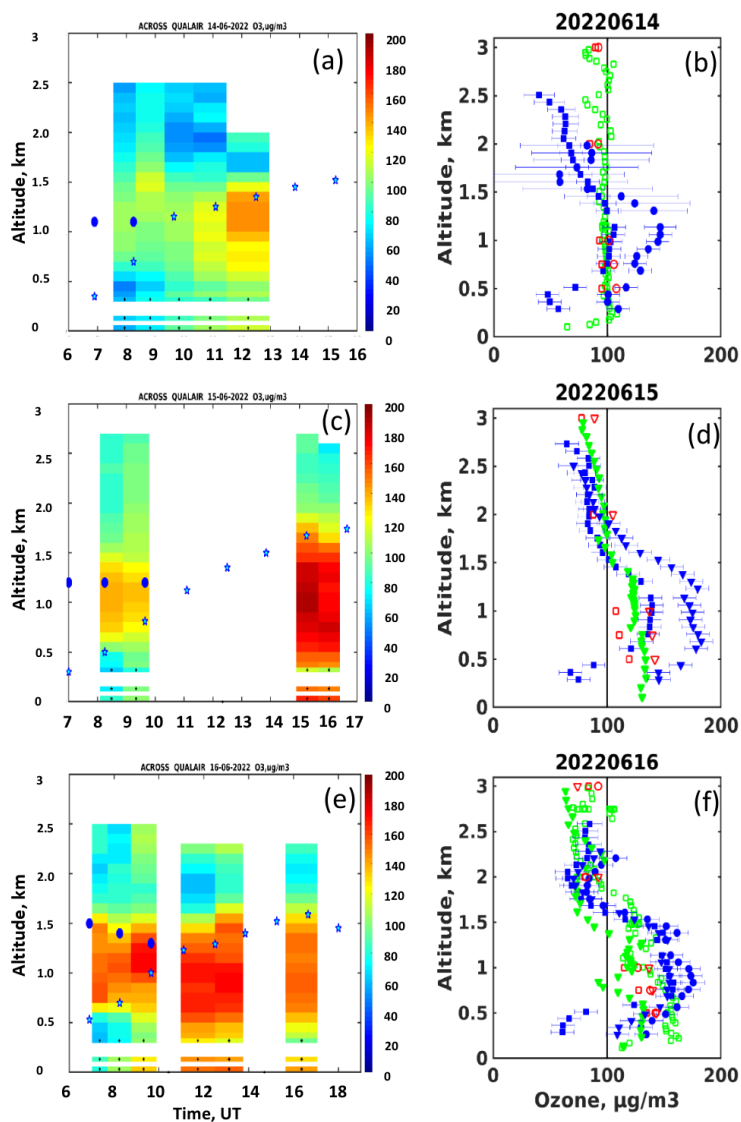


Figure 9. (left) Time-altitude O_3 concentration daytime evolution in $\mu\text{g}\cdot\text{m}^{-3}$ using DIAL above 300m and in-situ O_3 monitor below 300 m (pixel with black cross). The blue star and circle are the SLIM lidar PBLH and RLH. (right) O_3 vertical profiles in $\mu\text{g}\cdot\text{m}^{-3}$ for the DIAL (blue), the IAGOS aircraft (green) and the CAMS ensemble model (red) on June 14 (top), 15 (middle), 16 (bottom) 2022. Model data are shown at 6 UT (\square), 12 UT (\circ) and 18 UT (∇). The morning IAGOS data (\square) are before 5 UT, the afternoon IAGOS data (\blacktriangledown) are at 14 UT on June 15 and at 21 UT on June 16.

270 $80 \mu\text{g}\cdot\text{m}^{-3}$ are observed by the DIAL above 1.5 km on June 17 and 18 (Fig.10a, c) corresponding to the dust plume advection discussed in section 4.1. The IAGOS and CAMS vertical profiles above 2 km (Fig.10b,d) show also O_3 concentrations less than $80 \mu\text{g}\cdot\text{m}^{-3}$. The CAMS simulations at 2000 m (Fig.14) also show the advection of the low ozone streamer located over Brittany

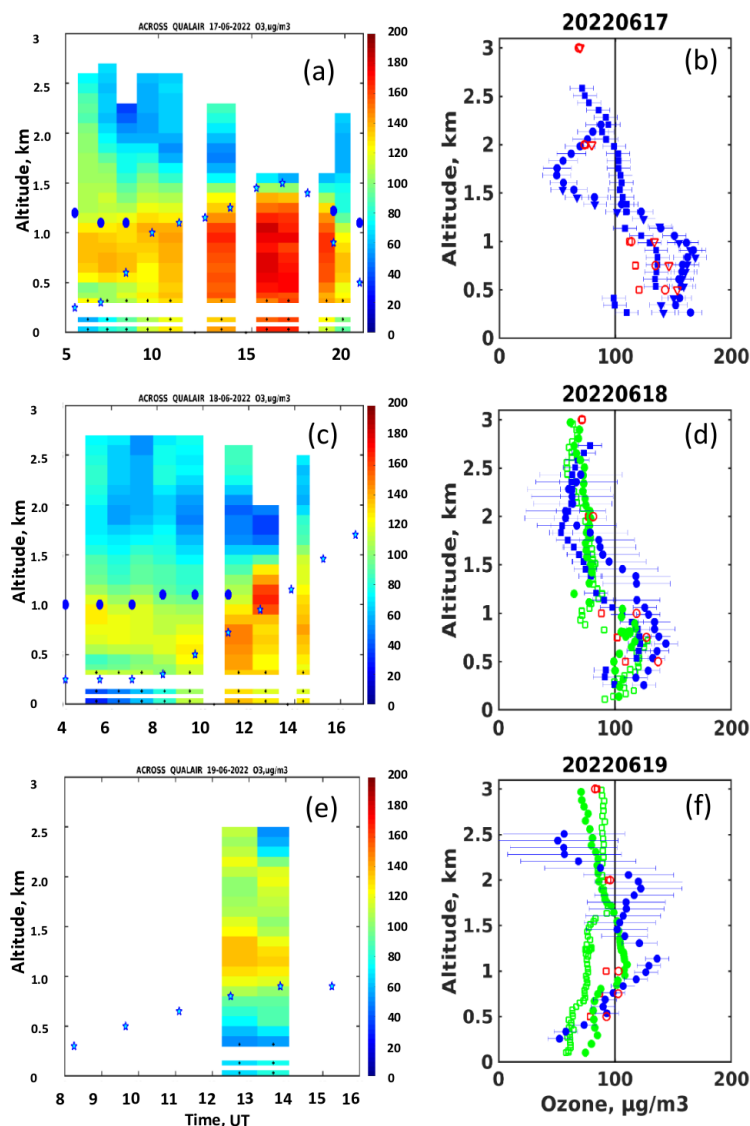


Figure 10. As Fig.9 for June 17, 18, 19 2022. The mid-day IAGOS data (●) is at 9 UT on June 18 and 14 UT on June 19.

and the English Channel on June 21 and east of Paris on June 17, implying that this ozone decrease in the free troposphere is indeed a regional feature not specific to the Paris city center. Second the June 22 ozone layer in the 1km-2.5km altitude layer (Fig.11c) is different from the other days with free tropospheric O_3 concentrations up to $130 \mu\text{g}\cdot\text{m}^{-3}$, while this layer doesn't mix very well with the surface layer during the day. Such a layer with concentration larger than $100 \mu\text{g}\cdot\text{m}^{-3}$ is not present in the CAMS vertical profile (Fig.11d) above the Paris area although there is an ozone streamer in the 18 UT CAMS simulation at 2 km with concentrations $> 110 \mu\text{g}\cdot\text{m}^{-3}$ moving across Northern France from East to West on June 21/22 (Fig.14). The 14

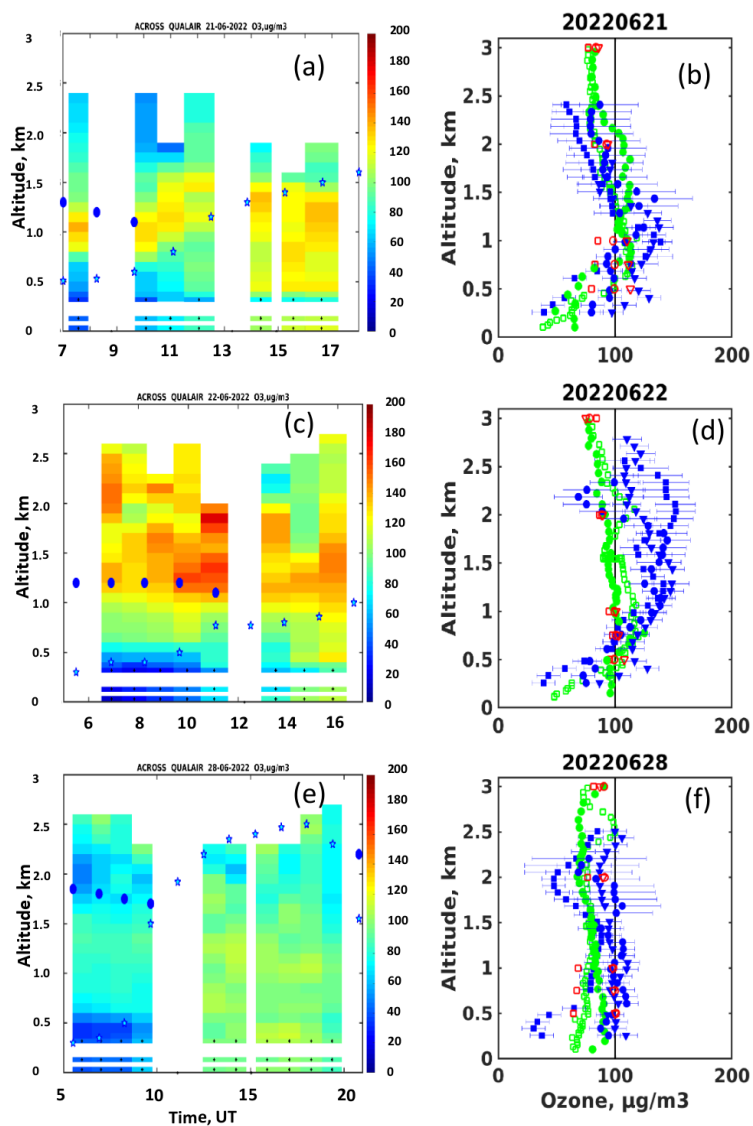


Figure 11. As Fig.9 for June 21, 22, 28, 2022. The mid-day IAGOS data (●) are at 14 UT on June 22 while they are at 10 UT on June 21, 28.

UT IAGOS profile (Fig.11d) also exhibits O₃ concentrations up to 120 µg.m⁻³ in a layer at 2 km, contrary to the other IAGOS profiles.

5 Discussion

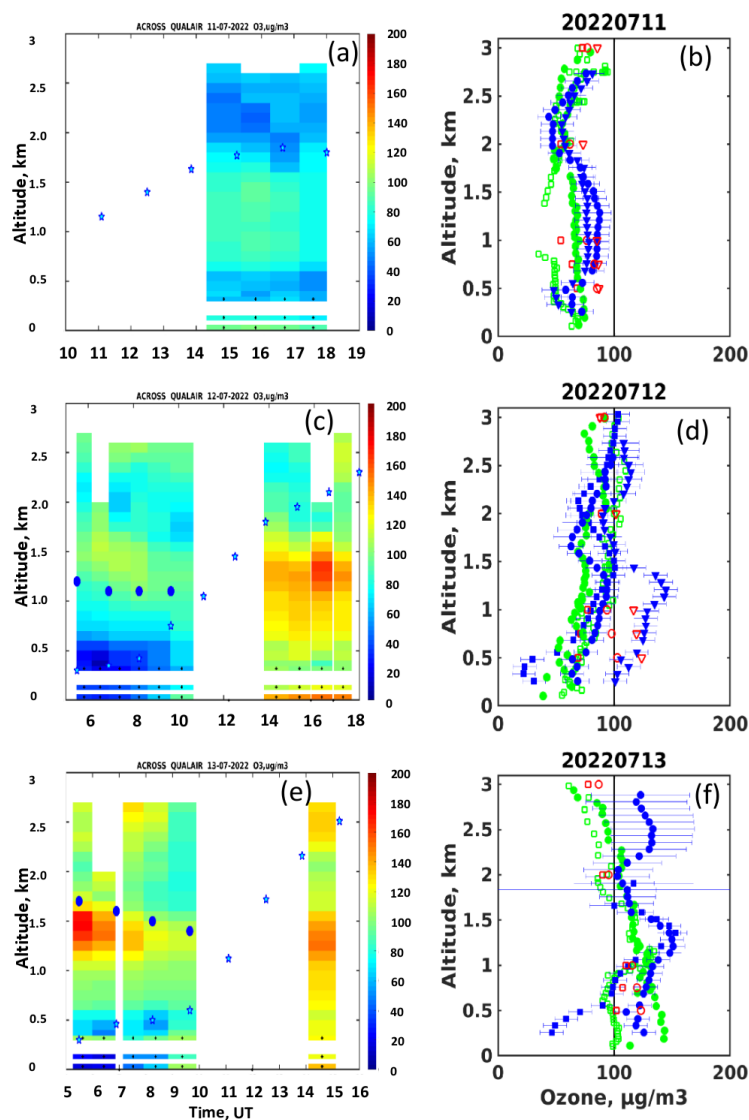


Figure 12. As Fig.9 for July 11 to 13, 2022. The mid-day IAGOS data (●) are at 14 UT on June 11 and 13 while they are at 10 UT on July 12.

5.1 Day to day variability of the O₃ lowermost tropospheric column: IASI, CAMS and ACROSS O₃ profiles

The IASI O₃ 0-3 km partial columns have been computed for the period 13 June – 13 July 2022 for both AM and PM overpasses. Comparisons between IASI O₃ 0-3 km partial column, ACROSS observations (IAGOS and DIAL) and CAMS simulations are shown in Fig.13. For IAGOS, DIAL and CAMS data, two partial columns have been calculated: the 0-3 km and the 1.2-3 km partial columns (dots and squares in Fig.13, respectively). The difference between those two columns corresponds to the 0-



1.2km column, called the near-surface column, where satellite observations are known to be less sensitive to ozone extreme values (Cuesta et al., 2013). All measurement days, whether or not they corresponded to pollution episodes, were considered in order to assess O₃ variability in the lowermost column during the ACROSS campaign from June 13 to July 14. All the hourly means of the DIAL and IAGOS observations made between 6 UT and 20 UT have been considered as well as the IASI morning and evening observations. The daily mean of the columns derived from the CAMS ensemble simulations are shown by the red solid lines in Fig.13.

From June 13 to July 14 2022, the IASI O₃ 0-3 km partial columns are in agreement with IAGOS, DIAL and CAMS O₃ 1.2-3km partial columns. The monthly averaged IASI O₃ 0-3 km partial column is 7.00 ± 1.40 DU, which is consistent with the averaged O₃ 1.2-3km partial columns derived from IAGOS (6.77 ± 0.99 DU), DIAL (7.38 ± 1.36 DU) and CAMS (6.95 ± 0.80 DU) over the same period (Table 2). This suggests that IASI is able to reproduce concentration and variability of ozone in the 1.2-3 km partial column during the ACROSS campaign.

DIAL measurements suggest that the diurnal variability of O₃ 0-3 km partial column reaches 5 DU while the 1.2-3km partial column reaches 2 DU during the ACROSS campaign (blue dots and squares in Fig.13), confirming the importance of monitoring ozone profiles at high temporal resolution throughout the day. The near-surface ozone columns, assessed by the difference between DIAL 0-3km and 1.2-3km, range from almost 10 DU on June 15, 16, and 17 in the afternoon, to less than 4 DU in the morning on June 27 and 29, and July 2, 4 and 5. For those last days, the AM IASI O₃ 0-3 km partial columns are higher than the ACROSS (IAGOS, DIAL, and CAMS) O₃ 1.2-3 km partial columns but are in agreement with the ACROSS O₃ 0-3 km column. For instance, the average of IASI columns measured on June 27 2022 at 10:00 (LT) is 9.07 DU, which is in excellent agreement with the integrated column (0-3 km) derived from IAGOS of 9.39 DU at 10:00 (LT), and DIAL of 9.73 DU at 7:00. This suggests that IASI O₃ satellite observations between 0-3km are in agreement with ACROSS data when near-surface ozone columns are lower than 4 DU. When O₃ near-surface columns (0-1.2 km) are higher (from 4 to 10 DU), then IASI only reproduces O₃ columns variability above the PBL. Therefore, IASI satellite measurements are able to accurately monitor O₃ lowermost columns between 0-3 km with a better agreement with the ACROSS dataset (IAGOS, DIAL, and CAMS) when O₃ located in the PBL is lower than 4DU.

5.2 Regional transport of the ozone layer

The potential emission sensitivity (PES) of a passive air tracer are calculated with the FLEXPART model version 9.02 initialized with the $1^\circ \times 1^\circ$ ECMWF operational meteorological analysis. The FLEXPART model is run backward over 72 hours with 17000 particles released in boxes 35 km by 35 km wide at different altitude ranges above the DIAL: 0-500m, 0.5-1.2km, 1.2-2.1km, 2.1-3.0km. The 0.5-1.2km and 2.1-3.0km PES maps are shown in Fig.S3 to S6 using a color scale in s for the vertically integrated residence time of the released particles. All the grid cell altitudes below 3km are cumulated to calculate the mean PES in the lowermost troposphere. Looking at the midday PES distributions of particles released either from the PBL or from the free troposphere, one can distinguish five horizontal advection patterns:



Table 2. Mean and standard deviation of O₃ partial columns (0-3km and 1.2-3km) in Dobson Unit (DU) derived from IAGOS, DIAL, CAMS, and IASI dataset during the ACROSS campaign between June 13 to July 13 2022.

Dataset	O ₃ column (DU)		Number of observations
	0 - 3 km	1.2 - 3 km	
IAGOS	11.56±1.93	6.77±0.99	49
DIAL	12.88±2.38	7.38±1.36	52
CAMS	12.00±1.77	6.95±0.80	32
IASI AM	7.75±1.37		19
IASI PM	6.25±0.98		19
IASI	7.00±1.40		38

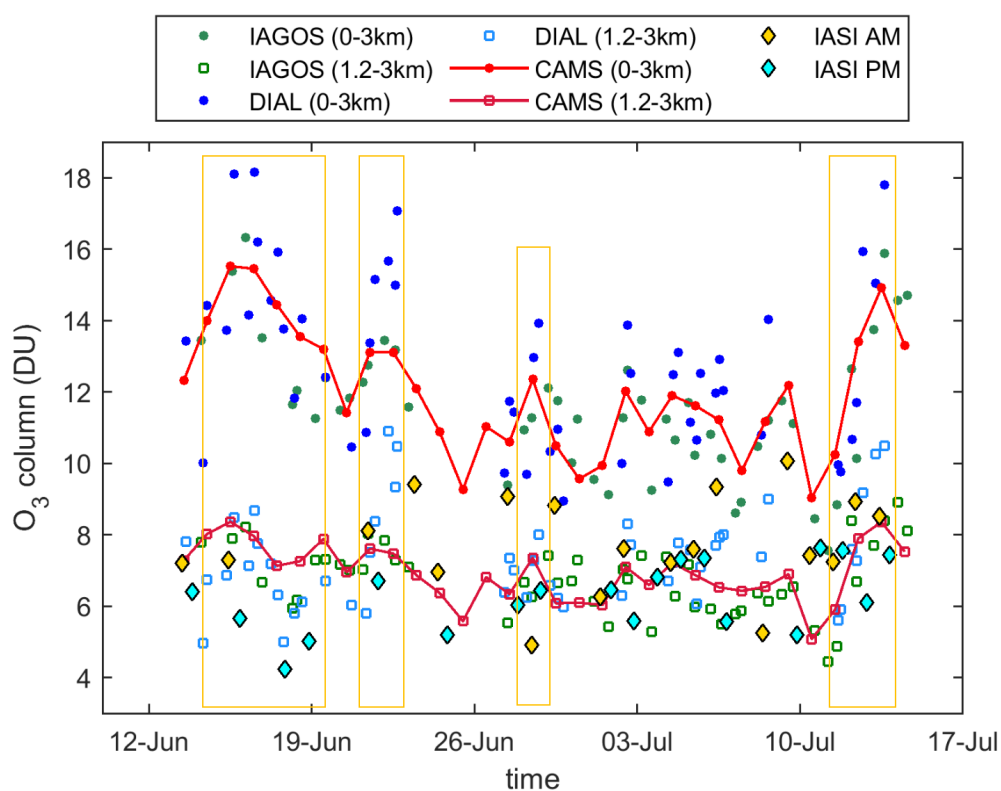


Figure 13. Comparison of tropospheric lowermost O₃ column derived from the ACROSS observations (DIAL in blue and IAGOS in green), CAMS data (in red), and IASI satellite observations (morning – yellow diamonds, and evening – cyan diamonds) calculated in the [48.84°N-49°N, 2°E-2.5°E] box between June 13 to July 13 2022. Circles and squares correspond to the 0-3km and 1.2-3km O₃ partial columns, respectively. The orange boxes show the pollution days discussed in section 4.

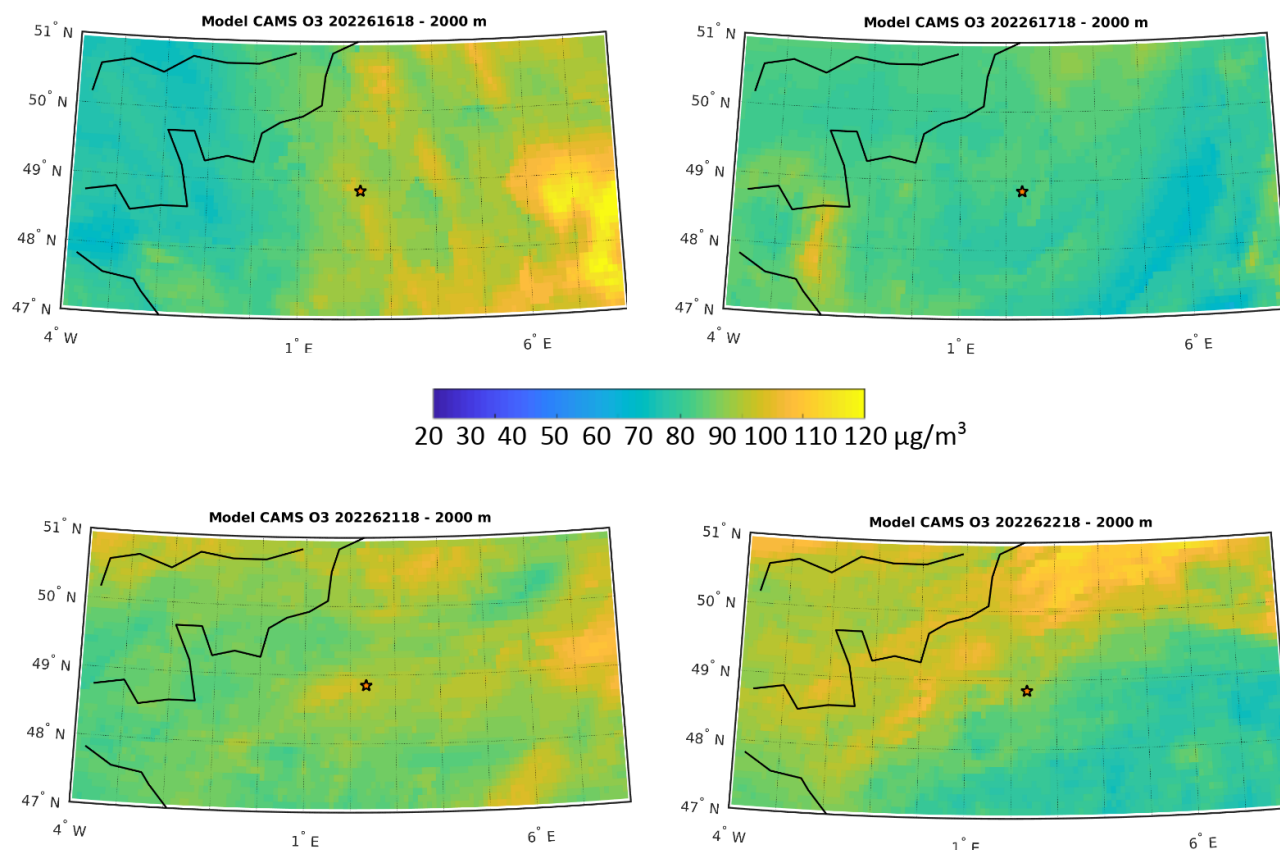


Figure 14. Ozone concentration distribution of the CAMS ensemble mean at 2000 m above Northern France on June 16 and 17 (top row) when low O₃ concentration and dust plume are seen by the Paris lidar above the PBL and on June 21 and 22 (bottom row) when high O₃ concentration layer and continental aerosol plume are seen by the Paris lidar above the PBL. The orange star and dark-blue triangle are respectively the DIAL position and the CDG airport. The color scale is O₃ concentration in µg.m⁻³.

- June 14, 15: Advection of continental air masses from Benelux and Germany below 1.2 km transport polluted air over Paris since the CAMS simulations (Fig.3) show high ozone plumes over these regions. The anticyclonic circulation below 2 km is also consistent with low PBLH observed in Paris during this time period. Moderate O₃ concentrations in the free troposphere are also consistent with a completely different circulation pattern above 2 km bringing cleaner air from the Atlantic ocean and the English Channel.
- June 16 to 18: In addition to the remaining anticyclonic conditions in the lowermost troposphere, long range transport of Saharan dust across Spain and the Atlantic coast is consistent with a dust aerosol plume just above the PBL measured by the SLIM lidar (section 4.1) and with a low ozone layer measured by the DIAL above 1.5 km in Paris. This southern advection above the PBL contributes also to the chemical composition of the PBL as there is a convergence of two streamers in the PES distribution below 1.2 km (Fig.S3 bottom row and S4 top row). On June 18, there is no longer



any difference in the PBL and the free troposphere circulation pattern (Fig.S4 middle row) in phase with the growing
330 contribution of the dust plume in the PBL chemical composition (Fig.6b).

– June 19 to 22: The origins of the air masses observed in Paris remain located in eastern France with limited long range
advection both in the PBL and in the free troposphere. This is consistent with an aerosol plume of European continental
pollution observed by the SLIM lidar on June 21 (Fig.7a) and the advection of high O₃ concentrations from eastern to
western France on June 22 (Fig.14).

335 – June 28: The influence of continental air masses is very limited on June 28 both in the PBL and in the free troposphere,
while a well defined westerly flow controls the chemical composition according to the elevated PES values above the
Atlantic Ocean (Fig.S5 bottom row). Such a circulation pattern explains both the elevated PBLH (no anticyclonic sub-
sidence in the free troposphere) and O₃ concentrations less than 100 µg.m⁻³ despite the elevated surface temperature of
Fig.2 on June 28 (advection of clean marine air masses).

340 – July 11-13: The horizontal advection shifts back to a northerly flow with transport of ozone poor air from Benelux
(Fig.4d) on July 11. This northerly flow is consistent with the Paris plume position in the southwestern part of Paris
region on July 12 (Fig.4e). On July 13 the flow shifts back to westerly flow especially above the PBL bringing back the
Paris plume above the city center and leading to high O₃ concentrations.

The position of the Paris ozone plume seen at 500 m in the CAMS simulations (Fig.3,4) corresponds very well with the cir-
345 culation pattern derived from the FLEXPART PES distribution below 1.2 km, except on June 17 when the plume is transported
to the northern part of the Paris region (Fig.3d) while the air mass origins are still from Eastern and Northern France (Fig.S4
top row).

5.3 Comparison of pollution episodes observed during ACROSS

Four pollution periods have been presented in the previous section. All 4 share conditions conducive to increasing O₃ con-
350 centrations in the lower troposphere above Paris: high temperatures (close to or above 30°C as shown in Fig.2), formation of
an ozone plume around Paris (see Fig.3,4, storage of ozone concentrations photochemically produced during the day within a
residual nocturnal layer (see Fig.9 to 10). The lowermost tropospheric O₃ columns also show extreme values above 13 DU for
these 4 episodes (see orange rectangles in Fig.13). However, there are significant differences in the formation of regional-scale
pollution plumes or the development of urban boundary layers over Paris to explain the variability of the extremes observed.

355 – June 14-18 case study: This period is characterized by a low PBLH < 1.5 km and advection of low ozone and a dust
plume in the free troposphere. Low ozone concentrations have been frequently observed within dust plume in western
Europe (Bonasoni et al., 2004; Andrey et al., 2014). Nevertheless the highest ozone concentrations (> 170 µg.m⁻³)
and lowermost tropospheric columns are found during this episode because European scale ozone photochemical pro-
duction took place in addition to local photochemistry in the Paris plume. Ozone pollution mitigation due to low ozone
360 concentrations in the dust plume took place only on June 18 when PBL and free troposphere mix more effectively.



- June 21-22 case study: The PBLH remains below 1.5 km while there is now an advection of continental plume with elevated ozone ($> 140 \mu\text{g}\cdot\text{m}^{-3}$) and aerosol concentrations in the free troposphere. The frequent occurrence of clouds in the mid-troposphere and lower surface temperatures than during the first case study explain less photochemical production within the Paris plume. The lowermost tropospheric columns are still above 14 DU because advection of the free tropospheric ozone layer just above the PBL compensate lower photochemical production within the PBL
- June 28 case study: Although the surface temperature is similar to the second case study, this pollution event is now characterized by elevated PBLH > 2.5 km and no advection of continental plumes above the PBL. Only the Paris plume contributes to the ozone photochemical production. This is consistent with O_3 concentrations $\leq 110 \mu\text{g}\cdot\text{m}^{-3}$ and lowermost tropospheric columns < 14 DU because ozone photochemical precursors will be diluted over a greater thickness. Lower cloud cover than during the second case study is not sufficient to compensate for dilution of ozone precursor emissions in the PBL.
- July 12-13 case study: The last pollution event is also characterized by elevated PBLH > 2.5 km and no advection of a continental plume, even though surfaces temperatures are as high as during the first pollution event. This is why the lowermost tropospheric columns are again above 14 DU, but contrary to the second case study elevated ozone concentrations $> 140 \mu\text{g}\cdot\text{m}^{-3}$ are mainly observed within the PBL.

6 Conclusions

Four ozone pollution events with surface concentrations above $100 \mu\text{g}\cdot\text{m}^{-3}$ and lowermost tropospheric columns greater than 14 DU have been encountered during the summer 2022 ACROSS campaign. In this work, vertical ozone profiles measured by a UV DIAL, aircraft (IAGOS) and surface stations at different elevations in the Paris area have been analyzed in synergy with CAMS model simulations at different level in the lowermost troposphere, with PBL diurnal evolution using a 808-nm microlidar SLIM and radiosoundings and with FLEXPART simulations of the regional scale advection in the Paris PBL. The contribution of the DIAL lidar is essential to picture the role of the residual layer ozone reservoir and that of advectations of continental pollution plumes or Saharan dust plumes above the boundary layer. We have shown in this study that the CAMS simulations of the Paris ozone plume are consistent with the measurements of the ozone vertical profiles and that the IASI satellite observations can capture the day to day variability of the 0-3 km lowermost ozone column if the contribution of the surface column below 1.2 km is lower than 4 DU. In addition to the well-known control of ozone photochemical production in the urban plume by the surface temperature, the cloud cover and the mixing between the surface layer (0 - 500 m) and the residual layer, this work has shown that the thickness of the PBL during the day and the advection of regional scale plumes above the PBL can significantly change the ozone concentrations. With similar cloud cover and air temperature, high ozone concentrations up to $180 \mu\text{g}\cdot\text{m}^{-3}$ are encountered during the day when PBLH is below 1.5 km, while they remain below $150 \mu\text{g}\cdot\text{m}^{-3}$ when PBLH increases above 2.5 km. Advection of ozone poor concentrations in the free troposphere during a Saharan dust event is able to mitigate the ozone photochemical production at the end of the first case study (June 18). On the other hand,



the advection of a continental pollution plume with high ozone concentrations $> 140 \mu\text{g}\cdot\text{m}^{-3}$ maintained high concentrations in the surface layer despite a decrease in temperatures and an increase in cloud cover (June 22).

395 Regarding the interaction between the urban layer dynamical development and the ozone plume formation during the day, this work is a first study. Further analyses are needed to characterize this interaction in the lowermost troposphere around Paris using additional measurements of wind field and turbulent mixing, e.g. radar and Doppler lidar observations carried out during ACROSS. The microlidar observations will be also improved in the future to monitor continuously both the ozone profile and the vertical structure of the atmospheric boundary layer. Finally the O_3 profiles presented in this paper in addition to aircraft
400 chemical observations of the urban plume carried out during the 2022 ACROSS campaign onboard the French ATR-42 aircraft will be very valuable datasets to validate future mesoscale simulations of the formation and transport of the ozone plume around Paris.

Code and data availability.

The IASI O_3 products processed with FORLI- O_3 are available at: <http://iasi.aeris-data.fr/O3/>, last access: 6 February 2024.

405 The AIRPARIF network ozone data have downloaded from <https://data-airparif-asso.opendata.arcgis.com/datasets/airparif-asso::2022-eiff3/> and <https://data-airparif-asso.opendata.arcgis.com/datasets/airparif-asso::2022-pa13/>

The QUALAIR station in-situ measurements (ozone, temperature) are available at <http://qualair.aero.jussieu.fr/qualair.php?menu=ozone&option=jussieu>

The IAGOS have been downloaded from the IAGOS-AERIS web site <https://iagos.aeris-data.fr/download/>

410 The CAMS ENSEMBLE model hourly ANALYSIS of O_3 concentration at 1 levels from 20220613-20220714 on Europe have been downloaded from the CAMS website <https://ads.atmosphere.copernicus.eu/cdsapp#!/dataset/cams-europe-air-quality-forecasts?tab=overview>

The DIAL data are available on the ACROSS campaign data base using the following keyword ACROSS-LATMOS-SU-QUALAIR- O_3 -profile-Lidar. The data base is hosted by the AERIS web site: <https://across.aeris-data.fr/catalogue/>

415 The SLIM lidar data are available at <http://qualair.aero.jussieu.fr/>

The radiosounding data are available at <https://doi.org/10.25326/> and the skew-T diagrams have been plotted using the python library MetPy <https://unidata.github.io/MetPy/latest/index.html>

The Meteo France meteorological data for the Luxembourg and Tour Eiffel stations can be downloaded from <https://meteo.data.gouv.fr/datasets/6569b51ae64326786e4e8e1a>

420 The FLEXPART code version 9.2 was downloaded from the FLEXPART wiki homepage <https://www.flexpart.eu/downloads> and the meteorological analysis data extraction needed to run the FLEXPART model have been carried out on the ECMWF ATOS data server using the flex-extract version 7.1.3 package downloaded from FLEXPART wiki homepage.

“ACROSS Ground Operation” National Programme to improve knowledge of chemical transformations in the atmosphere, the interaction between plant and human emissions, and their role on air quality.



425 *Author contributions.* G.Ancellet (GA) and F. Ravetta (FR) designed the work plan and are the PI of the DIAL. C. Viatte (CV) and
C.Cailteau-Fischbach (CCF) provided the infrastructure of the QUALAIR station and CCF was responsible of the lidar deployment. CV
and A. Boynard (AB) conducted the analysis of the lowermost tropospheric columns and of the IASI data. J. Pelon (JP) and Pascal Genau
designed the SLIM lidar and conducted the analysis of the PBL structure. P. Nedelec (PN) provided the IAGOS data. Julie Capo (JC) and
Axel Roy (AR) provided the meteorological soundings and contributed to the analysis the PBL dynamical development. GA processed the
430 DIAL data and conducted the overall data synthesis. All contributed to the paper preparation.

Competing interests. No competing interest

Acknowledgements. The work was supported by Sorbonne Université and OSU Ecce TERRA through funding for running the QUALAIR
Paris Station. IASI is a joint mission of EUMETSAT and the Centre National d'Etudes Spatiales (CNES, France). ULB-LATMOS is ac-
knowledged for the development of the FORLI retrieval algorithm, and the AC SAF project of the EUMETSAT for providing IASI O₃
435 data.

The authors would like to acknowledge the QUALAIR team and infrastructure for their scientific support (<https://qualair.fr/index.php/en/english/>)

The PANAME experimental component benefits from supports from the H2C 4-year project funded by the French national agency for
research (ANR) with the reference ANR-20-CE22-0013 and also from Météo-France and WMO as part of the Research Demonstration
440 Project for Paris Olympics 2024 coordinated by Valéry Masson, and from Institut Pierre Simon Laplace supporting both measurements
(SIRTA observatory and ACTRIS research infrastructure) and data management (AERIS national data and services center). The ACROSS
ground based observations have been supported by the CNRS/INSU LEFE-CHAT project "ACROSS Ground Operation National Programme
to improve knowledge of chemical transformations in the atmosphere, the interaction between plant and human emissions, and their role on
air quality".

445 The authors acknowledge the AERIS data infrastructure for providing access to the IASI-FORLI data, and for hosting the IAGOS and
ACROSS data base. The AIRPARIF Air Quality Agency is gratefully acknowledged for providing the ozone surface data for Paris 13
and Eiffel tower stations. The European Centre for Medium Range Weather Forecasts (ECMWF) is acknowledged for the provision of
meteorological analysis data and the FLEXPART development team is acknowledged for the provision of the FLEXPART 9.2 model version
used in this publication.

450 Dr. Christopher Cantrell, PI of the ACROSS campaign is also gratefully acknowledged for his support.



References

- Ancellet, G., Ravetta, F., 1998. Compact airborne lidar for tropospheric ozone: description and field measurements. *Appl. Opt.* 37, 5509–5521. URL: <http://ao.osa.org/abstract.cfm?URI=ao-37-24-5509>, doi:<https://doi.org/10.1364/AO.37.005509>.
- Ancellet, G., Ravetta, F., 2005. Analysis and validation of ozone variability observed by lidar during the ESCOMPTE-2001 campaign. *Atmospheric Research* 74, 435–459. URL: <https://www.sciencedirect.com/science/article/pii/S0169809504001425>, doi:<https://doi.org/https://doi.org/10.1016/j.atmosres.2004.10.003>.
- Andrey, J., Cuevas, E., Parrondo, M., Alonso-Pérez, S., Redondas, A., Gil-Ojeda, M., 2014. Quantification of ozone reductions within the saharan air layer through a 13-year climatologic analysis of ozone profiles. *Atmospheric Environment* 84, 28–34. URL: <https://www.sciencedirect.com/science/article/pii/S1352231013008595>, doi:<https://doi.org/https://doi.org/10.1016/j.atmosenv.2013.11.030>.
- 460 Antón, M., Loyola, D., Clerbaux, C., López, M., Vilaplana, J., Bañón, M., Hadji-Lazaro, J., Valks, P., Hao, N., Zimmer, W., Coheur, P., Hurtmans, D., Alados-Arboledas, L., 2011. Validation of the MetOp-A total ozone data from GOME-2 and IASI using reference ground-based measurements at the Iberian Peninsula. *Remote Sensing of Environment* 115, 1380–1386. URL: <https://www.sciencedirect.com/science/article/pii/S003442571100040X>, doi:<https://doi.org/https://doi.org/10.1016/j.rse.2011.01.018>.
- Bonasoni, P., Cristofanelli, P., Calzolari, F., Bonafè, U., Evangelisti, F., Stohl, A., Zauli Sajani, S., van Dingenen, R., Colombo, T., Balkanski, Y., 2004. Aerosol-ozone correlations during dust transport episodes. *Atmospheric Chemistry and Physics* 4, 1201–1215. URL: <https://acp.copernicus.org/articles/4/1201/2004/>, doi:<https://doi.org/10.5194/acp-4-1201-2004>.
- 465 Boynard, A., Clerbaux, C., Coheur, P.F., Hurtmans, D., Turquety, S., George, M., Hadji-Lazaro, J., Keim, C., Meyer-Arnek, J., 2009. Measurements of total and tropospheric ozone from IASI: comparison with correlative satellite, ground-based and ozonesonde observations. *Atmospheric Chemistry and Physics* 9, 6255–6271. URL: <https://acp.copernicus.org/articles/9/6255/2009/>, doi:<https://doi.org/10.5194/acp-9-6255-2009>.
- 470 Boynard, A., Hurtmans, D., Garane, K., Goutail, F., Hadji-Lazaro, J., Koukouli, M.E., Wespes, C., Vigouroux, C., Keppens, A., Pommereau, J.P., Pazmino, A., Balis, D., Loyola, D., Valks, P., Sussmann, R., Smale, D., Coheur, P.F., Clerbaux, C., 2018. Validation of the IASI FORLI/EUMETSAT ozone products using satellite (GOME-2), ground-based (Brewer–Dobson, SAOZ, FTIR) and ozonesonde measurements. *Atmospheric Measurement Techniques* 11, 5125–5152. URL: <https://amt.copernicus.org/articles/11/5125/2018/>, doi:<https://doi.org/10.5194/amt-11-5125-2018>.
- 475 Boynard, A., Hurtmans, D., Koukouli, M.E., Goutail, F., Bureau, J., Safieddine, S., Lerot, C., Hadji-Lazaro, J., Wespes, C., Pommereau, J.P., Pazmino, A., Zyrichidou, I., Balis, D., Barbe, A., Mikhailenko, S.N., Loyola, D., Valks, P., Van Roozendaal, M., Coheur, P.F., Clerbaux, C., 2016. Seven years of IASI ozone retrievals from FORLI: validation with independent total column and vertical profile measurements. *Atmospheric Measurement Techniques* 9, 4327–4353. URL: <https://amt.copernicus.org/articles/9/4327/2016/>, doi:<https://doi.org/10.5194/amt-9-4327-2016>.
- 480 Caputi, D.J., Faloona, I., Trousdell, J., Smoot, J., Falk, N., Conley, S., 2019. Residual layer ozone, mixing, and the nocturnal jet in California’s San Joaquin Valley. *Atmospheric Chemistry and Physics* 19, 4721–4740. URL: <https://acp.copernicus.org/articles/19/4721/2019/>, doi:<https://doi.org/10.5194/acp-19-4721-2019>.
- Couillard, M.H., Schwab, M.J., Schwab, J.J., Lu, C.H.S., Joseph, E., Stutsrim, B., Shrestha, B., Zhang, J., Knepp, T.N., Gronoff, G.P., 2021. Vertical Profiles of Ozone Concentrations in the Lower Troposphere Downwind of New York City During LISTOS 2018–2019. *Journal of Geophysical Research: Atmospheres* 126, e2021JD035108. URL: <https://agupubs.onlinelibrary.wiley.com/doi/abs/10.1029/2021JD035108>, doi:<https://doi.org/https://doi.org/10.1029/2021JD035108>,



- arXiv:<https://agupubs.onlinelibrary.wiley.com/doi/pdf/10.1029/2021JD035108>. e2021JD035108
2021JD035108.
- 490 Cuesta, J., Eremenko, M., Liu, X., Dufour, G., Cai, Z., Höpfner, M., von Clarmann, T., Sellitto, P., Foret, G., Gaubert, B., Beekmann, M., Orphal, J., Chance, K., Spurr, R., Flaud, J.M., 2013. Satellite observation of lowermost tropospheric ozone by multispectral synergism of IASI thermal infrared and GOME-2 ultraviolet measurements over Europe. *Atmospheric Chemistry and Physics* 13, 9675–9693. URL: <https://acp.copernicus.org/articles/13/9675/2013/>, doi:<https://doi.org/10.5194/acp-13-9675-2013>.
- Daum, P.H., Kleinman, L.I., Springston, S.R., Nunnermacker, L.J., Lee, Y.N., Weinstein-Lloyd, J., Zheng, J.,
495 Berkowitz, C.M., 2004. Origin and properties of plumes of high ozone observed during the Texas 2000 Air Quality Study (TexAQS 2000). *Journal of Geophysical Research: Atmospheres* 109. URL: <https://agupubs.onlinelibrary.wiley.com/doi/abs/10.1029/2003JD004311>, doi:<https://doi.org/https://doi.org/10.1029/2003JD004311>, arXiv:<https://agupubs.onlinelibrary.wiley.com/doi/pdf/10.1029/2003JD004311>.
- Drobinski, P., Saïd, F., Ancellet, G., Arteta, J., Augustin, P., Bastin, S., Brut, A., Caccia, J., Campistron, B., Cautenet, S., Colette, A., Coll,
500 I., Corsmeier, U., Cros, B., Dabas, A., Delbarre, H., Dufour, A., Durand, P., Guénard, V., Hasel, M., Kalthoff, N., C.Kottmeier, Lasry, F., Lemonsu, A., Lohou, F., Masson, V., Menut, L., Moppert, C., Peuch, V., Puygrenier, V., Reitebuch, O., Vautard, R., 2007. Regional transport and dilution during high-pollution episodes in southern France: Summary of findings from the Field Experiment to Constraint Models of Atmospheric Pollution and Emissions Transport (ESCOMPTE). *J. Geophys. Res.* 112. doi:<https://doi.org/10.1029/2006JD007494>.
- Dufour, G., Eremenko, M., Orphal, J., Flaud, J.M., 2010. IASI observations of seasonal and day-to-day variations of tropospheric ozone over
505 three highly populated areas of China: Beijing, Shanghai, and Hong Kong. *Atmospheric Chemistry and Physics* 10, 3787–3801. URL: <https://acp.copernicus.org/articles/10/3787/2010/>, doi:<https://doi.org/10.5194/acp-10-3787-2010>.
- Dupont, E., Pelon, J., Flamant, C., 1994. Study of the moist convective boundary layer structure by backscattering lidar. *Boundary-Layer Meteorology* 69, 1–25. URL: <https://doi.org/10.1007/BF00713292>, doi:<https://doi.org/10.1007/BF00713292>.
- Eremenko, M., Dufour, G., Foret, G., Keim, C., Orphal, J., Beekmann, M., Bergametti, G., Flaud, J.M.,
510 2008. Tropospheric ozone distributions over Europe during the heat wave in July 2007 observed from infrared nadir spectra recorded by IASI. *Geophysical Research Letters* 35. URL: <https://agupubs.onlinelibrary.wiley.com/doi/abs/10.1029/2008GL034803>, doi:<https://doi.org/https://doi.org/10.1029/2008GL034803>, arXiv:<https://agupubs.onlinelibrary.wiley.com/doi/pdf/10.1029/2008GL034803>.
- Flamant, C., Pelon, J., 1996. Atmospheric boundary-layer structure over the Mediterranean during a Tramon-
515 tane event. *Quarterly Journal of the Royal Meteorological Society* 122, 1741–1778. URL: <https://rmets.onlinelibrary.wiley.com/doi/abs/10.1002/qj.49712253602>, doi:<https://doi.org/https://doi.org/10.1002/qj.49712253602>, arXiv:<https://rmets.onlinelibrary.wiley.com/doi/pdf/10.1002/qj.49712253602>.
- Fowler, D., Amann, M., Anderson, R., Ashmore, M., Cox, P., Depledge, M., Derwent, D., Grennfelt, P., Hewitt, N., Hov, O., Jenkin, M.,
Kelly, F., Liss, P., Pilling, M., Pyle, J., Slingo, J., Stevenson, D., 2008. Ground-level ozone in the 21st century: Future trends, impacts and
520 policy implications. volume 15 of *Royal Society Science Policy Report*. 08 ed.
- Güsten, H., Heinrich, G., Sprung, D., 1998. Nocturnal depletion of ozone in the Upper Rhine Valley. *Atmospheric Environment* 32, 1195–
1202. URL: <https://www.sciencedirect.com/science/article/pii/S1352231097001957>, doi:[https://doi.org/https://doi.org/10.1016/S1352-2310\(97\)00195-7](https://doi.org/https://doi.org/10.1016/S1352-2310(97)00195-7).
- Hurtmans, D., Coheur, P.F., Wespes, C., Clarisse, L., Scharf, O., Clerbaux, C., Hadji-Lazaro, J., George, M., Turquety, S., 2012. FORLI radi-
525 ative transfer and retrieval code for IASI. *Journal of Quantitative Spectroscopy and Radiative Transfer* 113, 1391–1408. URL: <https://www>.



- sciencedirect.com/science/article/pii/S0022407312001008, doi:<https://doi.org/https://doi.org/10.1016/j.jqsrt.2012.02.036>. three Leaders in Spectroscopy.
- Inness, A., Ades, M., Agustí-Panareda, A., Barré, J., Benedictow, A., Blechschmidt, A.M., Dominguez, J.J., Engelen, R., Eskes, H., Flemming, J., Huijnen, V., Jones, L., Kipling, Z., Massart, S., Parrington, M., Peuch, V.H., Razinger, M., Remy, S., Schulz, M., Suttie, M., 2019. The CAMS reanalysis of atmospheric composition. *Atmospheric Chemistry and Physics* 19, 3515–3556. URL: <https://acp.copernicus.org/articles/19/3515/2019/>, doi:<https://doi.org/10.5194/acp-19-3515-2019>.
- Keppens, A., Lambert, J.C., Granville, J., Hubert, D., Verhoelst, T., Compernelle, S., Latter, B., Kerridge, B., Siddans, R., Boynard, A., Hadji-Lazaro, J., Clerbaux, C., Wespes, C., Hurtmans, D.R., Coheur, P.F., van Peet, J.C.A., van der A, R.J., Garane, K., Koukouli, M.E., Balis, D.S., Delcloo, A., Kivi, R., Stübi, R., Godin-Beekmann, S., Van Roozendael, M., Zehner, C., 2018. Quality assessment of the Ozone_cci Climate Research Data Package (release 2017) – Part 2: Ground-based validation of nadir ozone profile data products. *Atmospheric Measurement Techniques* 11, 3769–3800. URL: <https://amt.copernicus.org/articles/11/3769/2018/>, doi:<https://doi.org/10.5194/amt-11-3769-2018>.
- Klein, A., Ancellet, G., Ravetta, F., Thomas, J.L., Pazmino, A., 2017. Characterizing the seasonal cycle and vertical structure of ozone in Paris, France using four years of ground based LIDAR measurements in the lowermost troposphere. *Atmospheric Environment* 167, 603 – 615. URL: <http://www.sciencedirect.com/science/article/pii/S1352231017305186>, doi:<https://doi.org/https://doi.org/10.1016/j.atmosenv.2017.08.016>.
- Klein, A., Ravetta, F., Thomas, J.L., Ancellet, G., Augustin, P., Wilson, R., Dieudonné, E., Fourmentin, M., Delbarre, H., Pelon, J., 2019. Influence of vertical mixing and nighttime transport on surface ozone variability in the morning in Paris and the surrounding region. *Atmospheric Environment* 197, 92 – 102. URL: <http://www.sciencedirect.com/science/article/pii/S135223101830699X>, doi:<https://doi.org/https://doi.org/10.1016/j.atmosenv.2018.10.009>.
- Klett, J.D., 1985. Lidar inversion with variable backscatter/extinction ratios. *Appl. Opt.* 24, 1638–1643. URL: <http://ao.osa.org/abstract.cfm?URI=ao-24-11-1638>, doi:<https://doi.org/10.1364/AO.24.001638>.
- Lin, M., Fiore, A.M., Horowitz, L.W., Cooper, O.R., Naik, V., Holloway, J., Johnson, B.J., Middlebrook, A.M., Oltmans, S.J., Pollack, I.B., Ryerson, T.B., Warner, J.X., Wiedinmyer, C., Wilson, J., Wyman, B., 2012. Transport of Asian ozone pollution into surface air over the western United States in spring. *Journal of Geophysical Research: Atmospheres* 117. URL: <https://agupubs.onlinelibrary.wiley.com/doi/abs/10.1029/2011JD016961>, doi:<https://doi.org/https://doi.org/10.1029/2011JD016961>, arXiv:<https://agupubs.onlinelibrary.wiley.com/doi/pdf/10.1029/2011JD016961>.
- Ma, S., Tong, D., Lamsal, L., Wang, J., Zhang, X., Tang, Y., Saylor, R., Chai, T., Lee, P., Campbell, P., Baker, B., Kondragunta, S., Judd, L., Berkoff, T.A., Janz, S.J., Stajner, I., 2021. Improving predictability of high-ozone episodes through dynamic boundary conditions, emission refresh and chemical data assimilation during the Long Island Sound Tropospheric Ozone Study (LISTOS) field campaign. *Atmospheric Chemistry and Physics* 21, 16531–16553. URL: <https://acp.copernicus.org/articles/21/16531/2021/>, doi:<https://doi.org/10.5194/acp-21-16531-2021>.
- Marécal, V., Peuch, V.H., Andersson, C., Andersson, S., Arteta, J., Beekmann, M., Benedictow, A., Bergström, R., Bessagnet, B., Cansado, A., Chéroux, F., Colette, A., Coman, A., Curier, R.L., Denier van der Gon, H.A.C., Drouin, A., Elbern, H., Emili, E., Engelen, R.J., Eskes, H.J., Foret, G., Friese, E., Gauss, M., Giannaros, C., Guth, J., Joly, M., Jaumouillé, E., Josse, B., Kadygrov, N., Kaiser, J.W., Krajsek, K., Kuenen, J., Kumar, U., Liora, N., Lopez, E., Malherbe, L., Martinez, I., Melas, D., Meleux, F., Menut, L., Moinat, P., Morales, T., Parmentier, J., Piacentini, A., Plu, M., Poupkou, A., Queguiner, S., Robertson, L., Rouïl, L., Schaap, M., Segers, A., Sofiev, M., Tarasson, L., Thomas, M., Timmermans, R., Valdebenito, A., van Velthoven, P., van Versendaal, R., Vira, J., Ung, A., 2015. A regional air quality



- forecasting system over Europe: the MACC-II daily ensemble production. *Geoscientific Model Development* 8, 2777–2813. URL: <https://gmd.copernicus.org/articles/8/2777/2015/>, doi:<https://doi.org/10.5194/gmd-8-2777-2015>.
- 565 Mariage, V., Pelon, J., Blouzon, F., Victori, S., Geyskens, N., Amarouche, N., Drezen, C., Guillot, A., Calzas, M., Garracio, M., Wegmuller, N., Sennéchaël, N., Provost, C., 2017. IAOOS microlidar-on-buoy development and first atmospheric observations obtained during 2014 and 2015 arctic drifts. *Opt. Express* 25, A73–A84. URL: <https://opg.optica.org/oe/abstract.cfm?URI=oe-25-4-A73>, doi:<https://doi.org/10.1364/OE.25.000A73>.
- 570 Menut, L., Flamant, C., Pelon, J., Flamant, P.H., 1999. Urban boundary-layer height determination from lidar measurements over the Paris area. *Appl. Opt.* 38, 945–954. URL: <https://opg.optica.org/ao/abstract.cfm?URI=ao-38-6-945>, doi:<https://doi.org/10.1364/AO.38.000945>.
- Monks, P.S., Archibald, A.T., Colette, A., Cooper, O., Coyle, M., Derwent, R., Fowler, D., Granier, C., Law, K.S., Mills, G.E., Stevenson, D.S., Tarasova, O., Thouret, V., von Schneidemesser, E., Sommariva, R., Wild, O., Williams, M.L., 2015. Tropospheric ozone and its precursors from the urban to the global scale from air quality to short-lived climate forcer. *Atmospheric Chemistry and Physics* 15, 8889–8973. URL: <https://acp.copernicus.org/articles/15/8889/2015/>, doi:<https://doi.org/10.5194/acp-15-8889-2015>.
- 575 Neu, U., Künzle, T., Wanner, H., 1994. On the relation between ozone storage in the residual layer and daily variation in near-surface ozone concentration — a case study. *Boundary-Layer Meteorology* 69, 221–247. URL: <https://doi.org/10.1007/BF00708857>, doi:<https://doi.org/10.1007/BF00708857>.
- Nédélec, P., Blot, R., Boulanger, D., Athier, G., Cousin, J.M., Gautron, B., Petzold, A., Volz-Thomas, A., Thouret, V., 2015. Instrumentation on commercial aircraft for monitoring the atmospheric composition on a global scale: the IAGOS system, technical overview of ozone and carbon monoxide measurements. *Tellus B: Chemical and Physical Meteorology* doi:<https://doi.org/10.3402/tellusb.v67.27791>.
- O'Connor, E.J., Illingworth, A.J., Hogan, R.J., 2004. A technique for autocalibration of cloud lidar. *Journal of Atmospheric and Oceanic Technology* 21, 777 – 786. URL: https://journals.ametsoc.org/view/journals/atot/21/5/1520-0426_2004_021_0777_atfaoc_2_0_co_2.xml, doi:[https://doi.org/10.1175/1520-0426\(2004\)021<0777:ATFAOC>2.0.CO;2](https://doi.org/10.1175/1520-0426(2004)021<0777:ATFAOC>2.0.CO;2).
- 585 Pelon, J., Mallet, M., Mariscal, A., Goloub, P., Tanré, D., Bou Karam, D., Flamant, C., Haywood, J., Pospichal, B., Victori, S., 2008. Microlidar observations of biomass burning aerosol over Djougou (Benin) during African Monsoon Multidisciplinary Analysis Special Observation Period 0: Dust and Biomass-Burning Experiment. *Journal of Geophysical Research: Atmospheres* 113. URL: <https://agupubs.onlinelibrary.wiley.com/doi/abs/10.1029/2008JD009976>, doi:<https://doi.org/https://doi.org/10.1029/2008JD009976>, arXiv:<https://agupubs.onlinelibrary.wiley.com/doi/pdf/10.1029/2008JD009976>.
- 590 Pommier, M., Clerbaux, C., Law, K.S., Ancellet, G., Bernath, P., Coheur, P.F., Hadji-Lazaro, J., Hurtmans, D., Nédélec, P., Paris, J.D., Ravetta, F., Ryerson, T.B., Schlager, H., Weinheimer, A.J., 2012. Analysis of IASI tropospheric O₃ data over the Arctic during POLAR-CAT campaigns in 2008. *Atmospheric Chemistry and Physics* 12, 7371–7389. URL: <http://www.atmos-chem-phys.net/12/7371/2012/>, doi:<https://doi.org/10.5194/acp-12-7371-2012>.
- Ryerson, T.B., Andrews, A.E., Angevine, W.M., Bates, T.S., Brock, C.A., Cairns, B., Cohen, R.C., Cooper, O.R., de Gouw, J.A., Fehsenfeld, F.C., Ferrare, R.A., Fischer, M.L., Flagan, R.C., Goldstein, A.H., Hair, J.W., Hardesty, R.M., Hostetler, C.A., Jimenez, J.L., Langford, A.O., McCauley, E., McKeen, S.A., Molina, L.T., Nenes, A., Oltmans, S.J., Parrish, D.D., Pederson, J.R., Pierce, R.B., Prather, K., Quinn, P.K., Seinfeld, J.H., Senff, C.J., Sorooshian, A., Stutz, J., Sur-ratt, J.D., Trainer, M., Volkamer, R., Williams, E.J., Wofsy, S.C., 2013. The 2010 California Research at the Nexus of Air Quality and Climate Change (CalNex) field study. *Journal of Geophysical Research: Atmospheres* 118, 5830–5866. URL: <https://agupubs.onlinelibrary.wiley.com/doi/abs/10.1002/jgrd.50331>, doi:<https://doi.org/https://doi.org/10.1002/jgrd.50331>, arXiv:<https://agupubs.onlinelibrary.wiley.com/doi/pdf/10.1002/jgrd.50331>.
- 600



- Safieddine, S., Clerbaux, C., George, M., Hadji-Lazaro, J., Hurtmans, D., Coheur, P.F., Wespes, C., Loyola, D., Valks, P., Hao, N., 2013. Tropospheric ozone and nitrogen dioxide measurements in urban and rural regions as seen by IASI and GOME-2. *Journal of Geophysical Research: Atmospheres* 118, 10,555–10,566. URL: <https://agupubs.onlinelibrary.wiley.com/doi/abs/10.1002/jgrd.50669>, doi:<https://doi.org/https://doi.org/10.1002/jgrd.50669>, arXiv:<https://agupubs.onlinelibrary.wiley.com/doi/pdf/10.1002/jgrd.50669>.
- 605 Sarrat, C., Lemonsu, A., Masson, V., Guedalia, D., 2006. Impact of urban heat island on regional atmospheric pollution. *Atmospheric Environment* 40, 1743–1758. URL: <https://www.sciencedirect.com/science/article/pii/S1352231005010885>, doi:<https://doi.org/https://doi.org/10.1016/j.atmosenv.2005.11.037>.
- 610 Seinfeld, J., Pandis, S., 2016. *Atmospheric Chemistry and Physics: From Air Pollution to Climate Change*. Wiley. URL: https://books.google.fr/books?id=n_RmCgAAQBAJ.
- Senff, C.J., Alvarez II, R.J., Hardesty, R.M., Banta, R.M., Langford, A.O., 2010. Airborne lidar measurements of ozone flux downwind of Houston and Dallas. *Journal of Geophysical Research: Atmospheres* 115. URL: <https://agupubs.onlinelibrary.wiley.com/doi/abs/10.1029/2009JD013689>, doi:<https://doi.org/https://doi.org/10.1029/2009JD013689>, arXiv:<https://agupubs.onlinelibrary.wiley.com/doi/pdf/10.1029/2009JD013689>.
- 615 Stull, R., 1988. *An Introduction to Boundary Layer Meteorology*. Atmospheric and Oceanographic Sciences Library, Springer Netherlands. URL: <https://books.google.fr/books?id=eRRz9RNvNOKC>, doi:<https://doi.org/10.1007/978-94-009-3027-8>.
- Thouret, V., Marengo, A., Logan, J.A., Nédélec, P., Grouhel, C., 1998. Comparisons of ozone measurements from the MOZAIC airborne program and the ozone sounding network at eight locations. *Journal of Geophysical Research: Atmospheres* 103, 25695–25720. URL: <https://agupubs.onlinelibrary.wiley.com/doi/abs/10.1029/98JD02243>, doi:<https://doi.org/https://doi.org/10.1029/98JD02243>, arXiv:<https://agupubs.onlinelibrary.wiley.com/doi/pdf/10.1029/98JD02243>.
- 620 Vautard, R., Menut, L., Beekmann, M., Chazette, P., Flamant, P.H., Gombert, D., Guédalia, D., Kley, D., Lefebvre, M.P., Martin, D., Mégie, G., Perros, P., Toupance, G., 2003. A synthesis of the Air Pollution Over the Paris Region (ESQUIF) field campaign. *Journal of Geophysical Research: Atmospheres* 108. URL: <https://agupubs.onlinelibrary.wiley.com/doi/abs/10.1029/2003JD003380>, doi:<https://doi.org/https://doi.org/10.1029/2003JD003380>, arXiv:<https://agupubs.onlinelibrary.wiley.com/doi/pdf/10.1029/2003JD003380>.
- 625 Viatte, C., Gaubert, B., Eremenko, M., Hase, F., Schneider, M., Blumenstock, T., Ray, M., Chelin, P., Flaud, J.M., Orphal, J., 2011. Tropospheric and total ozone columns over Paris (France) measured using medium-resolution ground-based solar-absorption Fourier-transform infrared spectroscopy. *Atmospheric Measurement Techniques* 4, 2323–2331. URL: <https://amt.copernicus.org/articles/4/2323/2011/>, doi:<https://doi.org/10.5194/amt-4-2323-2011>.
- 630 Wagner, A., Bennouna, Y., Blechschmidt, A.M., Brasseur, G., Chabrilat, S., Christophe, Y., Errera, Q., Eskes, H., Flemming, J., Hansen, K.M., Inness, A., Kapsomenakis, J., Langerock, B., Richter, A., Sudarchikova, N., Thouret, V., Zerefos, C., 2021. Comprehensive evaluation of the Copernicus Atmosphere Monitoring Service (CAMS) reanalysis against independent observations: Reactive gases. *Elementa: Science of the Anthropocene* 9, 00171. URL: <https://doi.org/10.1525/elementa.2020.00171>, doi:<https://doi.org/10.1525/elementa.2020.00171>, arXiv:<https://online.ucpress.edu/elementa/article-pdf/9/1/00171/463928/elementa.2020.00171.pdf>.
- 635 Wespes, C., Hurtmans, D., Clerbaux, C., Boynard, A., Coheur, P.F., 2018. Decrease in tropospheric O₃ levels in the Northern Hemisphere observed by IASI. *Atmospheric Chemistry and Physics* 18, 6867–6885. URL: <https://acp.copernicus.org/articles/18/6867/2018/>, doi:<https://doi.org/10.5194/acp-18-6867-2018>.

<https://doi.org/10.5194/egusphere-2024-892>

Preprint. Discussion started: 30 April 2024

© Author(s) 2024. CC BY 4.0 License.



- 640 Zaveri, R.A., Berkowitz, C.M., Kleinman, L.I., Springston, S.R., Doskey, P.V., Lonneman, W.A., Spicer, C.W., 2003. Ozone production efficiency and NO_x depletion in an urban plume: Interpretation of field observations and implications for evaluating O₃-NO_x-VOC sensitivity. *Journal of Geophysical Research: Atmospheres* 108. URL: <https://agupubs.onlinelibrary.wiley.com/doi/abs/10.1029/2002JD003144>, doi:<https://doi.org/https://doi.org/10.1029/2002JD003144>, arXiv:<https://agupubs.onlinelibrary.wiley.com/doi/pdf/10.1029/2002JD003144>.